Physics of Fluids

RESEARCH ARTICLE | JULY 01 2026

Aerodynamic coupling and vibration modes in vortex-induced vibrations of side-by-side cylinder arrays

Andrei Fershalov ; Niell Elvin ; Mikhail Fershalov ; Daniel Struk ; Yang Liu

Physics of Fluids 38, 074101 (2026)
https://doi.org/10.1063/5.0334722

Aerodynamic coupling and vibration modes in vortex-induced vibrations of side-by-side cylinder arrays

Cite as: Phys. Fluids **38**, 074101 (2026); doi: 10.1063/5.0334722
Submitted: 19 March 2026 · Accepted: 10 June 2026 ·
Published Online: 1 July 2026

View Online Export Citation CrossMark

Andrei Fershalov, Niell Elvin, Mikhail Fershalov, Daniel Struk, and Yang Liu[a)]

AFFILIATIONS

Department of Mechanical Engineering, The City College of New York, New York, New York 10031, USA

[a)]Author to whom correspondence should be addressed: yliu7@ccny.cuny.edu

ABSTRACT

Wind-tunnel experiments were conducted to investigate vortex-induced vibrations (VIVs) of side-by-side arrays of two and three identical circular cylinders mounted on flexible beams. The gap-to-diameter ratio was varied over $0.025 \le G/D \le 4$. At large spacings, the response approached that of an isolated oscillator: $1 \le G/D \le 4$ for two cylinders and $2 \le G/D \le 4$ for three cylinders. At smaller spacings, wake coupling modified the lock-in response and produced distinct collective vibration modes. In the two-cylinder array, the cylinders oscillated either synchronously or 180° out of phase. In the three-cylinder array, additional states appeared, including cases where the two outer cylinders moved together while the middle cylinder moved oppositely and cases where the middle cylinder remained nearly stationary while the outer cylinders vibrated 180° out of phase. With increasing reduced velocity, these states transitioned toward in-phase motion. Decreasing G/D below 0.5 substantially increased both vibration amplitude and lock-in bandwidth, with maximum amplitudes reaching approximately three and four times the isolated-cylinder value for the two- and three-cylinder arrays, respectively. These results demonstrate that spacing-controlled wake coupling can amplify VIV response and broaden the operational bandwidth of multi-cylinder oscillator arrays for flow-energy harvesting applications.

NOMENCLATURE

A	Vibration amplitude (m)
$A^* = A/D$	Non-dimensional vibration amplitude
$C_L(t)$	Instantaneous lift coefficient
$\bar{C}_L$	Cycle-averaged lift coefficient
C_{piezo}	Piezoelectric capacitance (F)
c	Structural damping coefficient (N s/m)
D	Cylinder diameter (m)
$F_L(t)$	Fluid lift force (N)
f	Oscillation frequency (Hz)
$f_n = \sqrt{k/m}$	Natural frequency (Hz)
f_v	Vortex-shedding frequency (Hz)
$f^* = f/f_n$	Non-dimensional oscillation frequency
G	Gap between cylinder surfaces (m)
G/D	Gap-to-diameter ratio
k	Structural stiffness (N/m)
L	Cylinder span/length (m)
m	Structural (vibrating) mass (kg)
$m^* = m/(\rho\pi D^2 L/4)$	Mass ratio
$P_{\text{piezo,opt}}$	Optimal electrical power output (W)
P^*_{diss}	Dimensionless instantaneous damping power
P^*_{in}	Dimensionless instantaneous input power
$P^*_{\text{piezo,opt}}$	Non-dimensional optimal electrical power
$\bar{P}^*_{\text{diss}}$	Dimensionless mean damping power
$\bar{P}^*_{\text{in}}$	Dimensionless mean input power
R	Electrical load resistance (Ω)
$Re = U_\infty D/\nu$	Reynolds number
$SG = 2\pi^3 m^* \zeta/(U^*)^2$	Skop–Griffin parameter
$St = f_v D/U_\infty$	Strouhal number
t	Time (s)
$U^* = U_\infty/(f_n D)$	Reduced velocity
U_∞	Free-stream velocity (m/s)
$Y(t)$	Transverse displacement (m)
$Y^* = Y/D$	Non-dimensional displacement
θ_{piezo}	Electromechanical coupling coefficient
ν	Kinematic viscosity (m^2/s)

ρ	Fluid density (kg/m³)
$\zeta = c/\left(2\sqrt{km}\right)$	Damping ratio
$\tau = \omega_n t$	Non-dimensional time
φ	Phase angle (rad)
$\omega = 2\pi f$	Circular oscillation frequency (rad/s)
$\omega_n = 2\pi f_n$	Natural circular frequency (rad/s)

I. INTRODUCTION

Vortex-induced vibration (VIV) is a fundamental form of fluid–structure interaction that occurs when an elastically supported bluff body is exposed to flow. The flow separations on either side of the body produces an alternating vortex street in the wake, generating periodic aerodynamic forces on the structure. When the frequency of these forces approaches the natural frequency of the oscillator, a synchronization process known as *lock-in* occurs, potentially leading to large periodic motions.[1–3] The characteristics of this response are governed by the flow conditions, structural properties, and body geometry.[4]

Among bluff-body geometries, the circular cylinder has become the canonical model for studying VIV because it exhibits a well-defined vortex-shedding process and closely represents many practical structures subjected to cross-flow, such as marine risers, heat exchanger tubes, and bridge cables. Understanding the VIV response of circular cylinders, therefore, provides essential insight for predicting, controlling, and utilizing flow-induced oscillations in real engineering applications.

Extensive research over the past decades has examined the mechanisms governing VIV of isolated circular cylinders.[1–8] These studies have demonstrated that the system response is strongly influenced by parameters, such as mass ratio, structural damping, and cylinder size.[4] The mass ratio, defined as the ratio of the structural mass to the displaced fluid mass, represents one of the key parameters governing VIV behavior. For flexibly mounted cylinders oscillating in air, previous studies have shown that the vibration response depends strongly on the system's mass and damping characteristics. Higher mass ratios generally lead to reduced vibration amplitudes and narrower lock-in ranges, while lower mass and damping promote stronger fluid–structure coupling.[3,4,6]

Further investigation into the effects of the single-cylinder oscillator parameters, such as mass, stiffness, and cylinder diameter, was carried out in Ref. 9, where each parameter was varied independently to isolate its influence. The results revealed that system mass ratio plays a dominant role, significantly affecting both the vibration amplitude and the width of the lock-in regime. While the initiation of oscillations was found to be nearly independent of mass ratio, the termination and overall bandwidth of lock-in were strongly mass-dependent. In general, systems with lower mass and damping exhibited larger vibration amplitudes and broader lock-in ranges, highlighting the conditions favorable for maximizing the response of VIV-based energy harvesters.[9]

While much of the early research on VIV focused on preventing structural fatigue and instability, more recent studies have explored the potential of utilizing these self-excited oscillations for energy harvesting from fluid flows.[9–29] The periodic motion generated during lock-in provides a consistent source of mechanical energy that can be converted into electrical power through piezoelectric, electromagnetic, or electrostatic transduction mechanisms.[12,15] Experimental investigations of single, flexibly mounted circular cylinder harvesters[9] demonstrated that the harvested power scales with the square of the vibration amplitude, indicating that any increase in oscillation amplitude can substantially enhance energy output. The question of optimizing energy-harvesting efficiency has been discussed in several studies,[9,17] where the influence of system parameters and flow conditions on conversion performance was analyzed. Further efforts to improve energy-harvesting potential have involved geometric modifications to the cylinder,[26–29] for example, introducing a slit-offset configuration[27] to enhance the induced vibrations and thereby increase the harvested power. In addition to cylinder-based harvesters, recent studies have investigated wake- and flow-induced vibration energy harvesting using flexible flapper-based configurations, highlighting alternative mechanisms for extracting energy from unsteady bluff-body wakes.[30,31]

When multiple bluff bodies are placed close to one another, their wakes interact, creating complex flow patterns and vibration responses that are not present in isolated configurations. The nature of this interference depends strongly on the relative arrangement and spacing between cylinders. In a tandem configuration, where one cylinder is placed downstream of another along the flow direction, the interactions are primarily wake-driven, with the downstream cylinder influenced by the unsteady vortices shed from the upstream one.[32–38] In contrast, side-by-side arrangements exhibit direct cross-flow coupling between the gaps between cylinders, leading to biased gap flow, bistable wake behavior, and strong aerodynamic forces that can either suppress or amplify oscillations.[39–42]

For elastically mounted cylinders, this coupling becomes even more pronounced, as the flow-structure feedback promotes synchronized or phase-shifted motion depending on bluff-body spacing. Experimental studies[43] have shown that as the gap decreases, vibration amplitudes grow substantially, and at very small separations, the pair can behave as a single oscillating system with enhanced motion. These characteristics make side-by-side cylinder arrays particularly promising for improving the energy-harvesting efficiency of VIV systems.

Despite the demonstrated potential of cylinder arrays to enhance flow-energy harvesting, the available experimental data on the coupled wake dynamics and vibration characteristics of freely responding cylinder–oscillator arrays remain limited. In particular, the influence of inter-cylinder spacing on vibration amplitude, lock-in bandwidth, synchronization behavior, coupled vibration modes, and the resulting energy-harvesting performance is not yet well understood. To address this gap, the present study experimentally investigates the VIV response of finite-length side-by-side cylinder arrays exposed to uniform airflow. Using the isolated-cylinder response as a reference, two-cylinder pairs and three-cylinder arrays are examined over a systematic range of gap-to-diameter ratios to determine how spacing governs the interaction regime and overall system dynamics.

The two-cylinder pair configuration represents the simplest coupled array, in which each oscillator is influenced by the neighboring wake from one side. In contrast, the three-cylinder array introduces a higher level of flow and structural complexity: the middle cylinder is affected by wakes from both sides, while each outer cylinder interacts asymmetrically with the central oscillator and the surrounding wake field. This comparison between isolated, two-cylinder, and three-cylinder configurations allows the role of inter-cylinder spacing to be isolated and reveals collective vibration states that are not present in the single-cylinder system. Examining these representative cases provides insight into the mechanisms of aerodynamic coupling in finite-length oscillator arrays and their potential to amplify vibration amplitude and broaden operational bandwidth, defined here as the range of reduced velocities over which the system remains in the lock-in regime. The findings contribute to the design of more efficient VIV-based energy-harvesting systems and offer a foundation for future experimental and numerical investigations of multi-body fluid–structure interactions.

II. THEORETICAL BACKGROUND

For a stationary circular cylinder in uniform flow, the formation of periodic vortices in the wake occurs at a frequency f_v is typically characterized by the Strouhal number $St = \frac{f_v D}{U_\infty}$, where D is the cylinder diameter and U_∞ is the free-stream velocity. The shedding behavior and value of St depend primarily on the Reynolds number, $Re = \frac{U_\infty D}{\nu}$, which defines the flow regime based on the ratio of inertial to viscous forces (ν being the kinematic viscosity of the fluid). Over a wide range of subcritical Reynolds numbers, the Strouhal number remains nearly constant, providing a convenient descriptor of the vortex-shedding frequency for a fixed cylinder.

When the cylinder is allowed to vibrate transversely to the flow, the problem becomes considerably more complex due to the coupling between structural motion and wake dynamics. In this case, the system behavior is characterized by several additional dimensionless parameters, namely, reduced velocity, $U^* = \frac{U_\infty}{f_n D}$, which relates the free-stream velocity U_∞ to the cylinder diameter and natural frequency (i.e., $f_n = \sqrt{\frac{k}{m}}$) of the oscillator, where m is the structural mass and k is the stiffness; mass ratio, $m^* = \frac{m}{\rho\pi D^2 L/4}$, representing the ratio of the structural mass to the mass of the displaced fluid, where ρ is the fluid density and L is the cylinder length; damping ratio, $\zeta = \frac{c}{2\sqrt{km}}$, quantifying the effect of structural damping, where c is the damping coefficient.

The transverse motion of a flexibly mounted cylinder can be modeled as a single-degree-of-freedom (SDOF) oscillator subjected to a fluid lift force $F_L(t)$,

$$m\frac{\mathrm{d}^2Y(t)}{\mathrm{d}t^2} + c\frac{\mathrm{d}Y(t)}{\mathrm{d}t} + kY(t) = F_L(t), \tag{1}$$

where t is the time and Y is the cylinder displacement in the cross-flow direction.

Expressing the fluid force in terms of the lift coefficient, $F_L(t) = \frac{1}{2}\rho U_\infty^2 DLC_L(t)$, where $C_L(t)$ is the instantaneous lift coefficient, and introducing the dimensionless displacement $Y^* = Y/D$ and dimensionless time $\tau = \omega_n t$, with $\omega_n = 2\pi f_n$, the governing equation can be rewritten in nondimensional form as

$$\frac{\mathrm{d}^2Y^*(\tau)}{\mathrm{d}\tau^2} + 2\zeta\frac{\mathrm{d}Y^*(\tau)}{\mathrm{d}\tau} + Y^* = \left(\frac{1}{2\pi^3}\right)\left(\frac{1}{m^*}\right)(U^*)^2 C_L(\tau). \tag{2}$$

Equation (2) provides a convenient nondimensional framework for analyzing and comparing VIV responses across different systems and flow conditions. In this form, the coupled effects of the structural and fluid parameters are represented compactly by the reduced velocity U^*, mass ratio m^*, and damping ratio ζ. These parameters govern the onset, amplitude, and range of the lock-in regime, where the vortex shedding frequency f synchronizes with the structural natural frequency f_n and the frequency ratio $f^* = \frac{f}{f_n}$ tends to be very close to 1 for high mass ratio configurations.[3]

In steady-state conditions, the oscillations become harmonic; thus, the dimensionless transverse displacement can be written as

$$Y^*(\tau) = A^*\sin(\omega^*\tau) = A^*\sin(f^*\tau), \tag{3}$$

where $A^* = \frac{A}{D}$ is the dimensionless amplitude of oscillation, A is the vibration amplitude, $\omega^* = \frac{\omega}{\omega_n} = \frac{2\pi f}{2\pi f_n} = f^*$ is the dimensionless oscillation frequency (normalized by the structure's natural frequency).

At a fixed reduced velocity ($U^* = $ const), assuming that the system has reached steady-state conditions ($A^* = $ const), the solution of Eq. (2) can be expressed in terms of the vibration amplitude and phase angle φ,

$$A^* = \frac{(U^*)^2}{2\pi^3 m^*}\frac{\bar{C}_L}{\sqrt{\left(1-(f^*)^2\right)^2 + (2\zeta f^*)^2}}, \tag{4}$$

$$\tan(\varphi) = \frac{2\zeta f^*}{1-(f^*)^2}. \tag{5}$$

At resonance ($f^* = 1$), Eq. (5) indicates that the phase angle approaches $\varphi = 90^\circ$,

$$\tan(\varphi) = \frac{2\zeta}{0} \to \varphi = \frac{\pi}{2}, \tag{6}$$

and Eq. (4) simplifies to

$$A^* = \frac{(U^*)^2}{2\pi^3 m^*}\frac{1}{2\zeta}\bar{C}_L. \tag{7}$$

From the obtained solution, it follows that at resonance, the phase angle between the external aerodynamic force and the structural response approaches 90°. Under this condition, the analysis simplifies, allowing the definition of a reference lift coefficient, $\bar{C}_{L,\mathrm{ref}}$, which represents the exact lift magnitude required to balance structural damping at resonance.

In VIV, however, experimental observations show that the phase angle φ is not fixed at 90° but varies with system parameters, such as the reduced velocity U^* and the amplitude ratio A^*, within the lock-in regime.[3,6,44] Consequently, the actual lift coefficient $\bar{C}_L$ and the phase angle φ act jointly to provide the energy needed to sustain the oscillation.

If the reference lift coefficient corresponding to $\varphi = 90^\circ$ is known, the lift coefficient required to maintain the same vibration amplitude A^* at a different phase angle can be obtained from the principle of energy equivalence, by equating the mean power input from the fluid to the mean power dissipated through structural damping.

The instantaneous power dissipated by damping is

$$P^*_{\mathrm{diss}}(\tau) = 2\zeta\left(\frac{\mathrm{d}Y^*(\tau)}{\mathrm{d}\tau}\right)^2. \tag{8}$$

Assuming harmonic motion of the system [Eq. (3)], the average power dissipated per cycle is

$$\bar{P}^*_{\mathrm{diss}} = \frac{1}{T}\int_0^T P^*_{\mathrm{diss}}(\tau)\mathrm{d}\tau = \zeta(A^*f^*)^2. \tag{9}$$

The instantaneous input power is

$$P^*_{\text{in}}(\tau) = F_L(\tau)\frac{\mathrm{d}Y^*(\tau)}{\mathrm{d}\tau}. \quad (10)$$

Then, the average power input per cycle is

$$\bar{P}^*_{\text{in}} = \frac{1}{2\pi}\int_0^{2\pi} P^*_{\text{in}}(\tau)\mathrm{d}\tau = \frac{1}{2}\left(\frac{(U^*)^2\bar{C}_L}{2\pi^3 m^*}\right)A^* f^* \sin(\varphi). \quad (11)$$

For the steady state vibration with the resonance condition ($f^* = 1$), the average power input and power dissipated are equal, yielding

$$\bar{C}_L = \frac{4\pi^3 m^* \zeta A^*}{(U^*)^2 \sin(\varphi)}. \quad (12)$$

Introducing the Skop–Griffin parameter $SG = \frac{2\pi^3 m^* \zeta}{(U^*)^2}$, Eq. (7) can be rewritten as follows:

$$A^* = \frac{(U^*)^2}{2\pi^3 m^*}\frac{1}{2\zeta}\bar{C}_L \sin(\varphi) = \frac{1}{2SG}\bar{C}_L \sin(\varphi). \quad (13)$$

The Skop–Griffin parameter encapsulates the combined effects of mass ratio, structural damping, and reduced velocity on the VIV response. It appears inversely proportional to the amplitude ratio A^*, indicating that as SG parameter increases due to higher damping, greater mass, or lower flow velocity, the resulting oscillation amplitude correspondingly decreases, resulting in lower power input.

In the context of flow-energy harvesting, the main objective is to maximize the mechanical energy transferred from the fluid to the structure and convert it efficiently into electrical power. A commonly investigated technique employs piezoelectric transducers, which produce an electric potential when mechanically strained, as, for example, by VIV. Although numerous circuit configurations have been analyzed for power conditioning and extraction, a simplified model is often adopted in which the piezoelectric element is connected to a purely resistive load. This approach provides analytical tractability and has been widely used in both theoretical modeling and experimental validation.[9,10,45]

Under these assumptions, the expression for the optimal electrical power output of the piezoelectric harvester can be written as[9]

$$P_{\text{piezo,opt}} = \frac{\omega\theta^2_{\text{piezo}}A^2}{2C_{\text{piezo}}}, \quad (14)$$

where θ_{piezo} represents the electromechanical coupling coefficient and C_{piezo} is the piezoelectric capacitance.

The corresponding dimensionless power $P^*_{\text{piezo,opt}}$, can be obtained following the formulation in Ref. 9:

$$P^*_{\text{piezo,opt}} = P_{\text{piezo,opt}}\frac{C_{\text{piezo}}}{\omega_n\theta^2_{\text{piezo}}D^2} = \frac{1}{2}(A^*)^2\left(\frac{\omega}{\omega_n}\right). \quad (15)$$

Within the lock-in regime, typical for structures oscillating in air, the vortex-shedding frequency synchronizes with the structural natural frequency ($\omega = \omega_n$).[1] Under this resonance condition, Eq. (15) reduces to

$$P^*_{\text{piezo,opt}} = \frac{1}{2}(A^*)^2. \quad (16)$$

This result highlights that the harvested power increases proportionally with the square of the vibration amplitude ratio, implying that even small gains in oscillation amplitude can yield significant improvements in energy output.

The analytical relationships derived above establish a reference framework for nondimensionalizing the VIV response and estimating the energy-harvesting performance of an individual oscillator. Because these relations are formulated for a single flexibly mounted cylinder, they are not used here as a closed-form predictive model for the coupled dynamics of cylinder arrays. Instead, they provide common response parameters, such as A^*, U^*, and the dimensionless optimal power, for comparing the array configurations with the isolated-cylinder baseline. The influence of wake coupling, gap ratio, and synchronization behavior is determined experimentally from the measured amplitude, frequency, phase relationships, and vibration-mode maps.

III. MATERIALS AND METHODS

This section describes the experimental setup and procedures used to investigate the VIV response of two- and three-cylinder side-by-side arrays. The main objective of the experiments was to examine how the spacing between cylinders influences the vibration amplitude, lock-in bandwidth, phase behavior, and overall energy-harvesting potential.

The experimental system consists of a circular cylinder elastically supported to allow vibration in the transverse (cross-flow) direction when subjected to aerodynamic excitation. The energy harvester configuration follows the design reported in Ref. 9. In that single-cylinder experiment, a lightweight 3D-printed hollow cylinder made of polylactic acid (PLA) with internal rib reinforcement was mounted at the free ends of two slender cantilever beams (i.e., one attached at the top and one at the bottom), while the opposite beam ends were fixed to a rigid base [see Fig. 1(a)]. The cylinder was positioned upstream of the beams to ensure undisturbed exposure to the oncoming flow. In this configuration, the unsteady aerodynamic forces generated by periodic vortex shedding interact with the structural dynamics of the supporting beams, producing self-excited transverse oscillations. A representative example of the cylinder's vibration response is shown in Fig. 1(b).

It was shown in Ref. 9 that configurations with the smallest mass ratio m^* and damping ratio ζ produced the largest vibration amplitudes and the widest lock-in bandwidths, consistent with those reported in Refs. 3 and 6. The set of parameters for the energy harvester that yielded the maximum response in Ref. 9 was adopted in the present study as the baseline configuration.

The elastic support consists of two aluminum cantilever beams with a density of 2730 kg/m^3, an elastic modulus of 69 GPa, a width of $h_b = 12.5$ mm, a thickness of $t_b = 1.5$ mm, and a length of $l_b = 451$ mm, resulting in an effective stiffness of approximately 15.75 N/m for the system. The circular cylinder used in this configuration has a diameter of 40 mm, a spanwise length of 400 mm, and a total vibrating mass of 70 g, corresponding to a mass ratio of $m^* = 114$. The natural frequency of the combined cantilever-cylinder oscillator was measured from free-decay tests in quiescent air, i.e., at zero free-stream velocity, and was found to be $f_n = 2.44$ Hz. The structural damping ratio was measured as $\zeta = 0.15\%$. For the isolated single-cylinder case, this configuration produces the characteristic amplitude response reported in Ref. 9, with the corresponding response curve provided in the supplementary material (Fig. S1). The

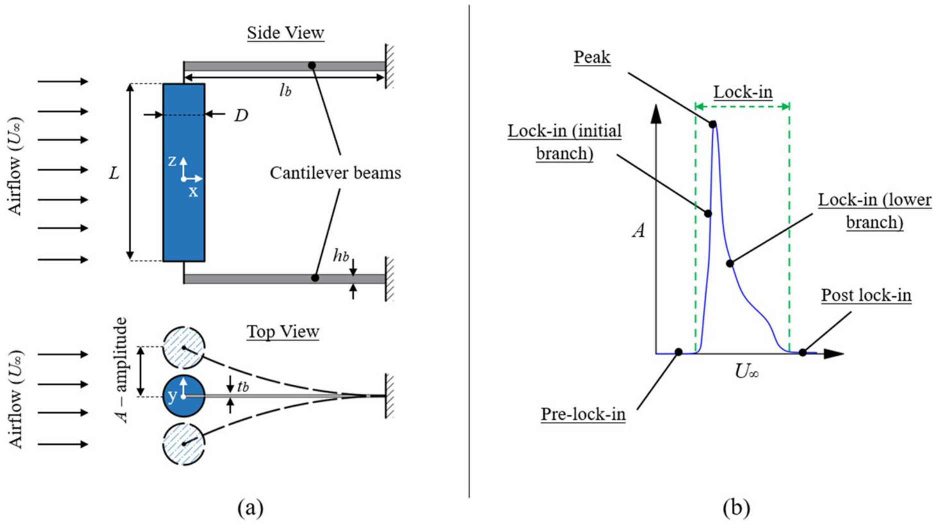

FIG. 1. (a) Schematic of a single VIV energy harvester, showing a finite-length circular cylinder mounted on elastic cantilever beams[9] and (b) schematic representation of a typical VIV amplitude response, illustrating the pre-lock-in, lock-in, and post-lock-in regimes.

experimental apparatus and data-processing procedure were benchmarked in the single-cylinder study reported in Ref. 9, where the measured onset of vibration, lock-in behavior, vibration-frequency response, and amplitude trends were shown to be consistent with established single-cylinder VIV observations.[1–3,6]

For this configuration, the isolated oscillator reached a peak non-dimensional amplitude of $A^* = 0.6$ at a reduced velocity of $U^* = 6.3$, with vibration initiating at $U^* = 5$ and ceasing at $U^* = 12.5$. This oscillator configuration was adopted from the single-cylinder parametric study in Ref. 9, in which the effects of beam length, stiffness, vibrating mass, and cylinder diameter were investigated. That study showed that the influence of beam length enters primarily through the resulting change in structural stiffness and natural frequency. The present configuration was selected because it produced the largest useful amplitude response within the target airflow velocity range of 1–4 m/s, which is representative of low-speed flow environments relevant to small-scale VIV energy harvesters, including building ventilation systems, roadside infrastructure, and ambient wind conditions. In the present study, the cylinder diameter and air properties were fixed; therefore, the Reynolds number varied only through the free-stream velocity and was not treated as an independent control parameter. The response is primarily presented in terms of reduced velocity, U^*, because this parameter directly captures the relationship between the flow speed and the structural natural frequency governing lock-in. Over the tested velocity range of 0.2–4 m/s, the corresponding Reynolds number range was approximately $Re = 5.3 \times 10^2 - 1.1 \times 10^4$. Thus, all measurements were conducted within the same low-speed air-flow regime for the selected oscillator geometry, while the main experimental variable was the gap-to-diameter ratio.

The two- and three-cylinder array configurations are shown in Fig. 2. In the present array experiments, the gap-to-diameter ratio was varied only by translating the complete oscillator units laterally relative to one another using an adjustable beam holder. Thus, the cantilever-beam length, stiffness, vibrating mass, and natural frequency of the individual oscillators were kept fixed while the gap G was varied.

The energy harvesters were installed on a rigid support frame constructed from 1.5 in. aluminum extruded profiles. Each harvester was mounted using two flexible beams positioned at the top and bottom ends of the cylinder. The corresponding cylinder aspect ratio was $AR = L/D = 10$; therefore, the cylinders should be regarded as finite-length bodies rather than ideal two-dimensional cylinders. To reduce aerodynamic interference from the support structure and mitigate end-region disturbances, the beams were placed outside the primary wake region and enclosed within streamlined protective hoods. This configuration, previously validated in Ref. 9, was shown to effectively reduce the influence of the support elements on the cylinder's dynamic response while maintaining structural rigidity. Finite-span effects for this type of oscillator were examined previously in Ref. 44. In the present array study, the aspect ratio, support arrangement, and end-region configuration were kept identical for all tested gap ratios, so the observed changes in amplitude, lock-in bandwidth, and vibration modes are interpreted as effects of inter-cylinder spacing and wake coupling under the same finite-length conditions. The experimental setup for the three-cylinder array, representative of both configurations studied, is shown in Fig. 3. The two-cylinder arrangement followed the same design and mounting principles.

All experiments were carried out in the Large-Scale Atmospheric Wind Tunnel at the City College of New York. A schematic of the facility is provided in the supplementary material (Fig. S2). This facility features an open-circuit, suction-type wind tunnel powered by a 20 b.h.p. electric motor with fine speed control, enabling free-stream velocities up to 15 m/s in the test section. To ensure flow uniformity, the setup was installed 7 m downstream from the entrance of the 8.4 m-long test section. The tunnel has a square cross section of $1.2 \times 1.2\,\text{m}^2$, with transparent side panels and a top viewing port to support flow visualization.

The contraction section includes a flow-conditioning assembly consisting of a honeycomb element followed by three layers of fine steel screens. This arrangement effectively straightens the inlet flow and reduces large-scale disturbances, resulting in a highly uniform velocity profile with turbulence intensity maintained below 0.1% at the highest operating speed of the test section.[46] The blockage ratio,

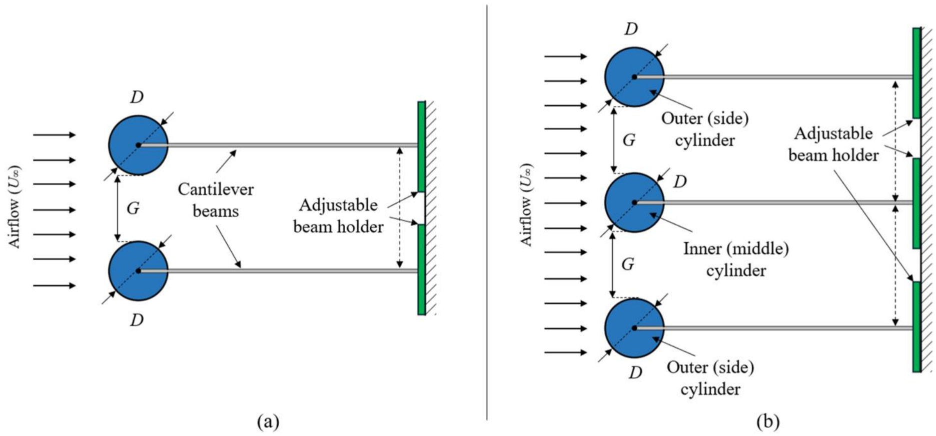

FIG. 2. Energy harvester configurations: (a) two cylinders array and (b) three cylinders array.

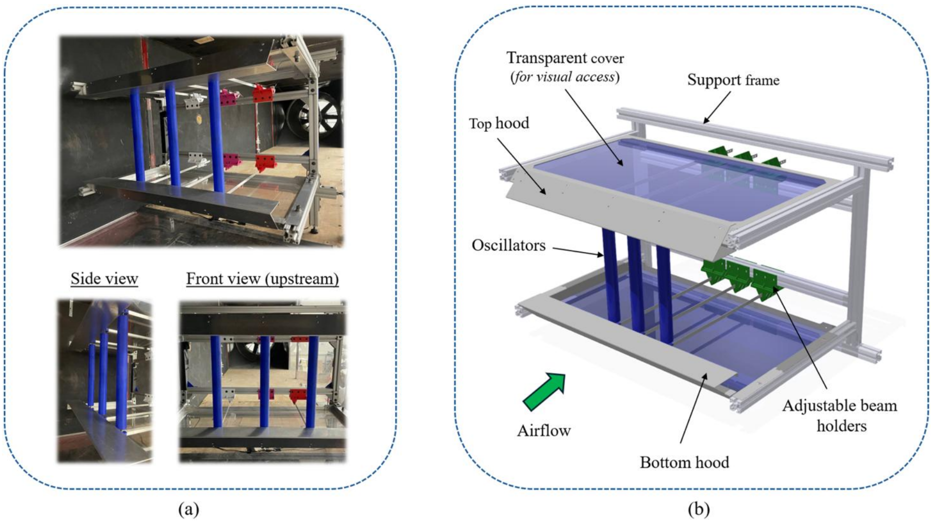

FIG. 3. Experimental setup for the three-cylinder array: (a) photograph of the assembled system within the wind tunnel and (b) 3D model showing the geometric arrangement and mounting configuration.

defined as the ratio of the model's projected frontal area to the cross-sectional area of the wind tunnel test section, was 8.5%. This level of blockage remains within the generally accepted limit of approximately 10%, below which subsonic wind tunnel testing is not expected to introduce significant flow interference or measurement bias.[47]

High-speed imaging was performed using a NOVA R3-4K camera in conjunction with Photron FASTCAM Viewer (PFV4) software, capturing 4096×2304 pixel resolution at 500 fps. The camera frame rate was sufficient to resolve both the structural oscillation and the relevant wake dynamics. The measured natural frequency of the oscillator was $f_n = 2.44$ Hz, and the VIV frequency remained close to this value during lock-in, corresponding to approximately 205 image frames per vibration cycle. A DHOM-H-532-1000 laser provided 532 nm wavelength green-light illumination, with beam intensity modulated via a DC power supply adjustable between 0 and 5 V. To enhance visibility of flow structures, a Magnum 1200 fog generator using JEM PRO-FOG fluid was employed to produce dense vapor droplets.

Each energy harvester was equipped with a strain gauge affixed near the clamped end of one of the aluminum beams to measure strain induced by the cylinder's motion. Calibration was conducted to establish the relationship between the strain-gauge output voltage and the transverse displacement of the cylinder axis. Following the procedure used in Ref. 9, known static loads were applied in the transverse direction, and the corresponding cylinder displacements were recorded. A total of nine calibration points were used for each oscillator: four in the positive direction, one at zero load, and four in the negative direction. The calibration showed a linear relationship between applied force and displacement, as well as between strain-gauge output and displacement, with coefficients of determination $r^2 > 0.999$ for all cases. The slope of the force–displacement curve was used to determine the static stiffness, while the voltage–displacement calibration was used to convert the dynamic strain-gauge signal into cylinder displacement during wind tunnel testing.

The strain gauge was interfaced with a strain indicator (Model MM120-001469, Micro-Measurements Inc.), and the signal was digitized using a National Instruments NI-6008 data acquisition card, with data collected in MATLAB at a sampling rate of 1000 Hz. This sampling rate was sufficient to resolve the relevant structural and wake-related frequencies. The Nyquist frequency of the acquisition system was 500 Hz, which is well above the structural vibration frequency.

To determine the natural frequency of each harvester, free vibration tests were conducted. Matching the natural frequencies across all harvesters was essential for consistent performance. Because of minor variations in stiffness, mass, and manufacturing tolerances, fine-tuning was achieved by adjusting the mass of each harvester. The natural frequencies were tuned to agree within ± 0.01 Hz, requiring mass corrections of no more than 2 g.

The spacing between cylinders is characterized using the gap-to-diameter ratio, G/D, where G denotes the surface-to-surface distance between adjacent cylinders. Under this definition, $G/D = 0$ corresponds to cylinders in the direct contact. The present study investigated two- and three-cylinder side-by-side arrays over a range of nominal spacings from $G/D = 0$ to $G/D = 4$, covering the regimes in which gap-flow instability, wake interference, and bistable behavior have been reported in the previous studies.[39–43] Because physical contact between cylinders introduces friction that affects the vibration dynamics, true $G/D = 0$ was not used in practice. Instead, the smallest achievable spacing without surface contact was $G/D = 0.025$, corresponding to a 1 mm gap. For the three-cylinder configuration, the two gaps were set to the same nominal value for all tests in order to maintain a geometrically symmetric array. In practice, small alignment and gap-setting uncertainties are unavoidable; therefore, the symmetry referred to here should be interpreted as nominal geometric symmetry rather than perfect dynamic symmetry. The vibration modes and phase relationships reported below were determined from the measured displacement signals of the three cylinders rather than imposed by symmetry assumptions.

The wind tunnel velocity was calibrated prior to testing using a calibrated hot-wire anemometer to establish the relationship between fan speed and free-stream velocity. During the array experiments, the free-stream velocity was monitored using a Pitot tube connected to a DSA5000 pressure scanner with an integrated data acquisition system. The pressure signal was sampled at 1000 Hz and used to calculate the free-stream velocity. The Pitot-tube measurements showed good agreement with the hot-wire calibration over the tested velocity range.

During testing, the free-stream velocity was increased in increments of 0.02 m/s. After each velocity change, the oscillators were allowed to reach steady-state motion before data acquisition. Using the measured damping ratio $\zeta = 0.15\%$ and natural frequency $\omega_n = 15.3$ rad/s, the decay time constant was estimated as $1/(\zeta\omega_n) \approx 44$ s. To ensure complete stabilization of the response, a conservative waiting period of 120 s was applied at every step. Steady-state was verified by examining the amplitude envelope over roughly 150 vibration cycles and confirming the absence of any systematic drift in amplitude (assessed through a linear trend check of the peak-amplitude sequence). After stabilization, strain-gauge data were recorded over a 60 s interval, corresponding to approximately 150 cycles of oscillation.

The main experimental uncertainties were associated with displacement calibration, frequency resolution, phase determination, and velocity-step discretization. The displacement uncertainty of the strain-gauge calibration was approximately ± 1 mm, corresponding to an uncertainty in amplitude ratio of $\Delta A^* \approx \pm 0.025$. The vibration frequency was obtained from 60 s displacement records, giving a nominal spectral resolution of $1/60 \approx 0.017$ Hz, or approximately $\Delta(f/f_n) \approx 0.007$ when normalized by f_n. The relative phase between cylinders was determined from the measured displacement signals; with a sampling rate of 1000 Hz, the time resolution corresponds to approximately 0.9° at the dominant vibration frequency. The free-stream velocity was varied in increments of 0.02 m/s, corresponding to a reduced-velocity resolution of approximately $\Delta U^* \approx 0.2$. Consequently, regime-boundary locations in the mode maps should be interpreted within this reduced-velocity resolution.

In summary, the experimental methodology described above establishes a controlled and repeatable framework for examining the VIV response of two- and three-cylinder side-by-side arrays. The combination of a precisely tunable structural support system, accurate strain-based displacement measurements, and carefully defined geometric configurations enables systematic investigation of how cylinder–cylinder spacing and wake coupling influence vibration amplitude, lock-in behavior, and energy-harvesting capability. The validated experimental framework enables the analysis presented in Sec. IV, where the vibration responses and flow-structure dynamics of the cylinder arrays are discussed.

IV. RESULTS AND DISCUSSION

The results presented in Secs. IV A–IV D describe the vibration response of the two- and three-cylinder side-by-side arrays as the free-stream velocity is varied for different gap ratios. For each spacing, the vibration amplitude, dominant frequency, and relative phase between cylinders were determined from the measured displacement signals, allowing the lock-in range and coupled vibration modes to be identified. The measured vibration frequency remained very close to the natural frequency of the individual oscillator, $f_n = 2.44$ Hz, throughout the lock-in regime for all tested gap ratios and vibration modes. This indicates that the VIV response was frequency-locked to the natural frequency of the combined cantilever-cylinder system, consistent with classical VIV behavior for high-mass-ratio oscillators in air[1–3] and with the hot-wire wake-frequency measurements reported for the same baseline oscillator in Ref. 9. Therefore, the discussion below focuses mainly on the amplitude response, lock-in bandwidth, and phase relationships between neighboring cylinders.

A. Two-cylinder array

For clarity, the experimental results are presented separately for the ranges $1 \le G/D \le 4$ and $0 \le G/D \le 1$. In addition, the two cylinders exhibited symmetric responses across all tested spacings, with identical trends in amplitude, onset, and cessation of oscillations. To avoid redundancy, the results are presented using the vibration amplitude of one cylinder from the pair, which fully represents the behavior of both cylinders for all G/D values considered.

The experimental results for the range $1 \le G/D \le 4$ are presented in Fig. 4(a), showing the vibration amplitude as a function of reduced velocity and capturing the full pre-lock-in, lock-in, and post-lock-in behavior of the two-cylinder array. At $G/D = 4$, the vibration response of each cylinder closely matches the isolated single-cylinder response reported in Ref. 9, indicating negligible wake coupling at this spacing. Therefore, the $G/D = 4$ curve in Fig. 4(a) is used as the isolated-cylinder reference for comparison with smaller gap ratios. As the spacing is reduced from $G/D = 4$ to $G/D = 1$, the response begins to deviate gradually from the isolated case. The onset of lock-in remains essentially unchanged across this range, but the

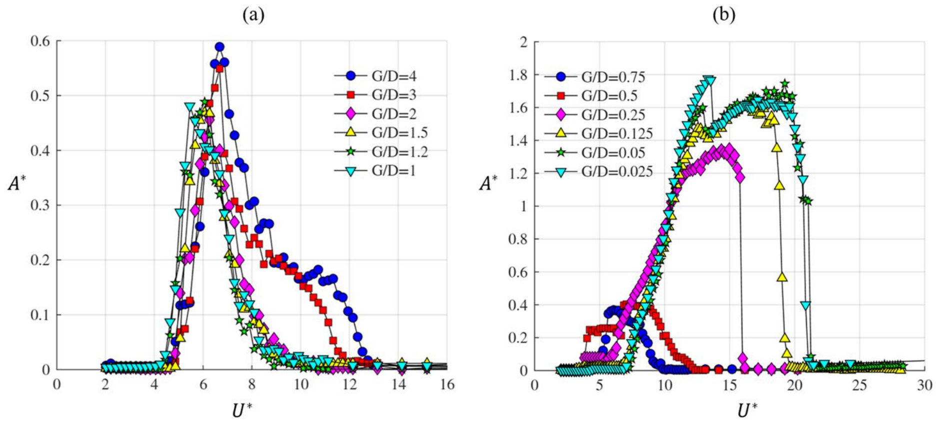

FIG. 4. Amplitude ratio vs reduced velocity for two cylinders arranged side by side (a) $1 \leq G/D \leq 4$ and (b) $0 < G/D < 1$. The $G/D = 4$ case coincides with the isolated single-cylinder response and is, therefore, used as the isolated-cylinder reference.

termination of lock-in shifts to lower reduced velocities. The peak non-dimensional amplitude also decreases slightly with decreasing G/D, consistent with modest hydrodynamic damping introduced by emerging wake interference. A small shift in the reduced velocity corresponding to the peak amplitude is observed as well, reflecting subtle changes in how vortex shedding synchronizes with the structural motion as the cylinders are brought closer together.

The amplitude response as a function of reduced velocity for gap ratios in the range $0 < G/D < 1$ is presented in Fig. 4(b). It is clearly seen that reducing the gap ratio below $G/D = 1$ leads to a pronounced change in the dynamic response of the two-cylinder array. For spacings within $0.5 \leq G/D < 1$, the peak amplitude remains below that of the isolated single-cylinder case, and the lock-in bandwidth is only mildly affected. However, when the gap is reduced to $G/D = 0.25$ and smaller, both the vibration amplitude and the extent of the lock-in region increase substantially. The most significant amplification occurs at the smallest tested spacing, $G/D = 0.025$, where the system reaches a peak amplitude of $A^* = 1.8$ and exhibits a markedly broadened lock-in interval. In this configuration, oscillations initiate at a lower reduced velocity ($U^* = 4.5$) and persist up to $U^* = 21$, nearly doubling the operational range compared to the isolated cylinder.

To further illustrate how spacing influences the vibration response, Fig. 5(a) shows the variation of the peak amplitude ratio A^*_{peak} as a function of the gap ratio G/D.

As the spacing decreases from $G/D = 4$ to $G/D = 1$, the peak amplitude gradually declines from $A^*_{\text{peak}} = 0.6$ to $A^*_{\text{peak}} = 0.48$. This decreasing trend continues to a minimum at $G/D = 0.75$. Below this spacing, however, the behavior changes: at $G/D = 0.5$, the amplitude rises slightly, though it remains below the isolated-cylinder value, while for $G/D < 0.5$, the system exhibits a clear amplification of the vibration response. The strongest enhancement occurs at the smallest tested spacing, $G/D = 0.025$, where the peak amplitude reaches $A^*_{\text{peak}} = 1.8$.

In addition to the peak amplitude, the lock-in bandwidth also provides a key measure of how spacing influences the system response. Figure 5(b) shows the variation of $\Delta U^* = U^*_{\text{end}} - U^*_{\text{start}}$ as a function of the gap ratio G/D.

A pronounced increase in bandwidth is observed for small gaps ($G/D \leq 0.5$), indicating that closely spaced cylinders experience more sustained fluid–structure coupling as the flow velocity increases. At these spacings, the oscillations persist over an extended range of reduced velocities, reflecting the strong aerodynamic interaction between the wakes. In contrast, for larger gaps, the bandwidth remains comparable to that of the isolated cylinder.

For reference, the isolated single-cylinder oscillator exhibits a lock-in bandwidth of approximately $\Delta U^* \approx 7.5$. In the two-cylinder pair configuration, the bandwidth at $G/D = 0.5$ is similar to this value, whereas the smallest tested spacing ($G/D = 0.025$) reaches $\Delta U^* = 16.5$, more than doubling the velocity range over which synchronized oscillations persist. This substantial expansion of the lock-in interval highlights how strong wake coupling at small spacings modifies the stability and extent of the periodic response.

To better understand the physical origin of these trends, the vibration response is next examined in terms of the coupled oscillation modes that emerge as the gap ratio decreases. For spacings down to $G/D \approx 1$, the system exhibits only gradual deviations from the isolated-cylinder response, characterized as a *weak-interaction regime*, in which wake interference is present but does not fundamentally alter the nature of the oscillation. However, once the gap becomes sufficiently small ($G/D < 1$), the wake of each cylinder interacts strongly with the other, producing abrupt changes in the vibration characteristics and altering the structure of the shared flow field. This marks the onset of the *strong-interaction regime*, within which the coupled system no longer behaves as two independent oscillators but instead supports distinct, spacing-dependent vibration modes.

Within this strong-interaction regime, the two-cylinder array supports distinct coupled vibration modes that do not appear at larger spacings. At the onset of lock-in, the cylinders oscillate 180° out of phase with one another, a motion referred to hereafter as the *anti-phase mode*. As the reduced velocity increases, the system transitions into an *in-phase mode*, where both cylinders move synchronously with nearly zero phase difference. This in-phase motion persists through the remainder of the lock-in interval and continues until oscillations decay in the post-lock-in regime. The emergence and evolution of these modes reflect the rapid changes in the shared wake topology and the intensification of aerodynamic coupling as the gap ratio decreases. For clarity, the two observed vibration modes are shown in Figs. 6(a) and 6(b).

Beyond the vibration measurements themselves, the underlying wake interactions associated with these modes can be interpreted in the context of previously documented interference patterns for

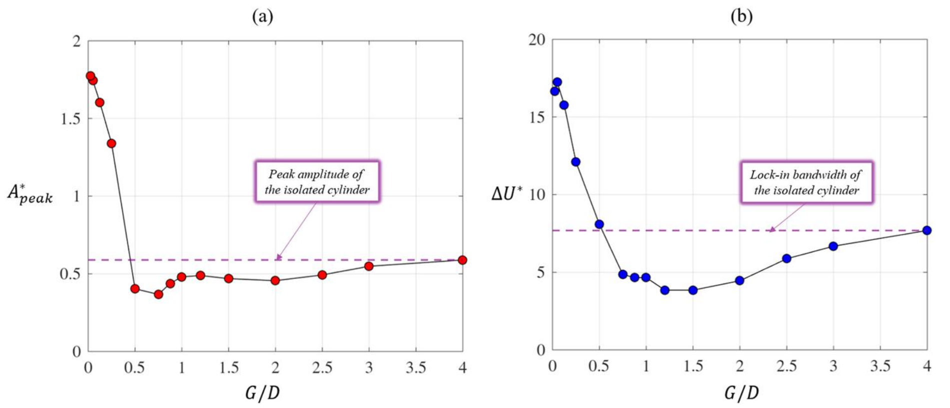

FIG. 5. (a) Peak amplitude ratio A^*_{peak} and (b) lock-in bandwidth ΔU^*, as functions of gap ratio G/D for two cylinders arranged side by side.

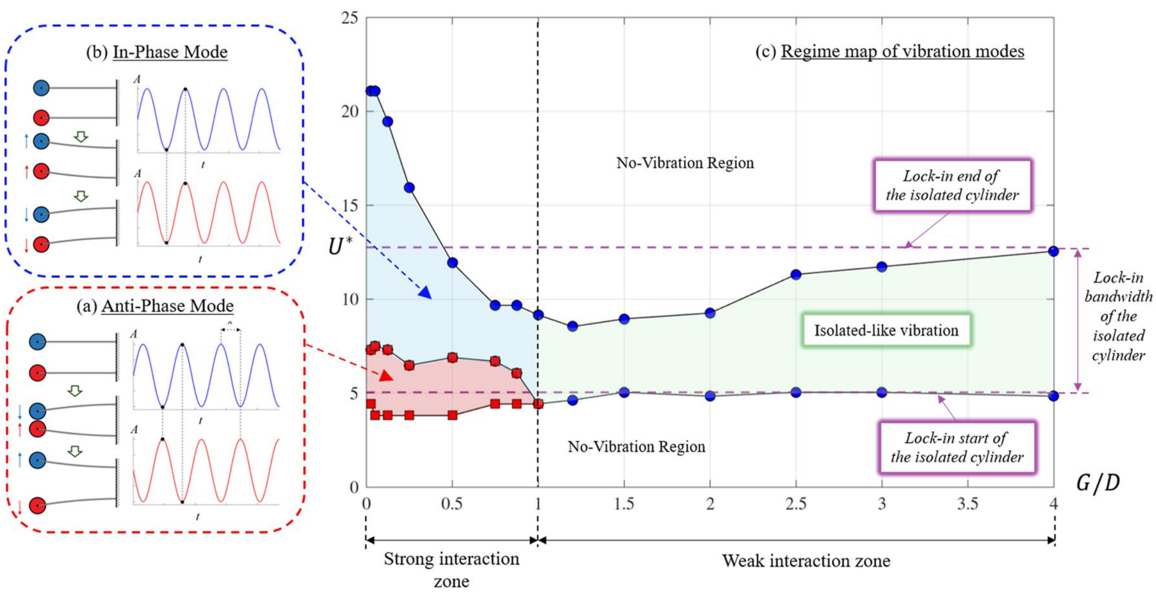

FIG. 6. Vibration modes and regime map for two side-by-side circular cylinders within the strong-interaction regime: (a) opposite-phase (anti-phase) oscillation; (b) in-phase oscillation; and (c) regime map showing the occurrence of vibration modes.

side-by-side cylinders. The interference regions relevant to two-cylinder configurations are summarized in the regime map shown in Fig. 6(c), which provides a useful framework for classifying the observed mode transitions and for comparing the present results with established flow regimes reported in earlier studies.[39–43] The boundaries in the regime map were determined from the discrete velocity sweep. At each tested velocity, the displacement signals of the cylinders were analyzed to determine whether sustained vibration was present and, when present, to classify the relative phase between cylinders. The onset and cessation of lock-in were identified when the steady periodic strain-gauge signal became distinguishable from, or returned to, the noise level. The transition between anti-phase and in-phase modes was determined from the measured phase difference between the two cylinder displacement signals. Because the free-stream velocity was increased in increments of 0.02 m/s, the corresponding reduced-velocity resolution was $\Delta U^* \approx 0.2$. The boundary lines in Fig. 6(c) should, therefore, be interpreted as experimental regime-transition guides based on the discrete velocity sweep.

Figure 6(c) synthesizes the spacing-dependent behavior of the two-cylinder array by mapping the onset and cessation of oscillation together with the observed vibration modes. For gap ratios $1 \le G/D \le 4$, the cylinders fall within a weak-interaction range, where their responses closely mirror the isolated-cylinder case. In this spacing interval, vibration consistently begins at $U^* = 5$, and the primary effect of decreasing G/D is a gradual reduction in the velocity at which oscillations cease, shifting from $U^* = 12.5$ at $G/D = 4$ to $U^* = 9$ at $G/D = 1$.

Below $G/D = 1$, the system transitions into the strong-interaction regime, where spacing directly governs the mode of vibration and the extent of the lock-in interval. Here, oscillations initiate slightly earlier than in the isolated case, typically within $U^* = 3.5 - 4.5$, and the cylinders first exhibit anti-phase motion before transitioning to synchronous in-phase vibration as the velocity increases. The velocity at which this mode transition occurs remains relatively consistent, around $U^* = 6.5 - 7.0$, for all gaps $G/D \leq 0.5$. These spacing-dependent variations in onset, cessation, and mode occurrence provide the structural framework needed to interpret the amplitude and bandwidth trends presented earlier and serve as a basis for later discussion of their implications for flow-energy harvesting.

These results demonstrate that bringing two cylinders into close proximity fundamentally alters the VIV response through strong hydrodynamic coupling. While the isolated cylinder reached a peak non-dimensional amplitude of $A^*_{\text{peak}} = 0.6$, the smallest spacing tested ($G/D = 0.025$) produced amplitudes up to $A^*_{\text{peak}} = 1.8$, a threefold increase. Because the optimal power output of a VIV-based harvester scales with the square of the amplitude ratio, this amplification corresponds to roughly a ninefold increase in potential energy extraction per oscillator.

In addition to the increase in vibration amplitude, small gap ratios resulted in a substantial enlargement of the lock-in bandwidth. The tightly spaced configuration exhibited a lock-in interval of $\Delta U^* = 16.5$, nearly twice that of the isolated cylinder ($\Delta U^* \approx 7.5$). This extended synchronization range enables effective vibration, and therefore, energy harvesting over a broader range of flow velocities, improving robustness under variable or unsteady flow conditions.

Overall, the two-cylinder experiments show that wake-induced coupling can act as an effective passive mechanism for enhancing vibration amplitude and prolonging sustained oscillation. At the same time, the sensitivity of the response to spacing underscores the necessity of carefully selecting inter-cylinder separation, as moderate gaps may suppress amplitude or reduce bandwidth.

The insights gained from the two-cylinder pair configuration motivate extending the investigation to a three-cylinder side-by-side array. The presence of a central cylinder introduces additional interference pathways and asymmetric wake coupling, enabling the study of more complex vibration modes and their implications for multi-oscillator energy-harvesting systems.

B. Three-cylinder array

Having established the effects of wake coupling in the two-cylinder arrangement, the analysis is now extended to a three-cylinder array. Introducing a third cylinder alters the interaction topology, creating a central body influenced simultaneously by wakes from both sides and two outer cylinders whose dynamics depend asymmetrically on the behavior of the central cylinder. This configuration enables exploration of multi-directional wake interference and additional coupled vibration modes that cannot arise in two-body systems, offering deeper insight into collective oscillation behavior in multi-cylinder arrays.

Similar to the two-cylinder pair, the three-cylinder array initially exhibits weak wake interference as the spacing is reduced; however, the departure from isolated-cylinder behavior occurs at larger spacing because the central cylinder interacts with wakes from both neighbors. When the spacing is reduced from $G/D = 4$ to $G/D = 2$, subtle wake interactions appear: the onset of lock-in remains unchanged, but the termination shifts to lower reduced velocities, and the peak amplitude decreases slightly, consistent with mild hydrodynamic interference.

Figure 7(a) shows the amplitude response as a function of reduced velocity for the three-cylinder array across this range of relatively weak spacing effects ($2 \leq G/D \leq 4$). The smallest spacing at which the three-cylinder array still behaves in an isolated-like manner is $G/D = 2$, in contrast to the two-cylinder case where this persists down to $G/D = 1$. This earlier departure from isolated behavior occurs because the central cylinder is simultaneously influenced by wakes from both neighboring bodies, resulting in stronger hydrodynamic coupling at larger gaps than in the two-body configuration.

When the gap ratio is reduced below $G/D = 2$, the interaction between the cylinders intensifies. In this range, the amplitude response and the extent of the lock-in interval change much more rapidly with spacing, and the array begins to exhibit several distinct coupled vibration patterns not present at larger gaps. These changes reflect the increasingly complex vortex interactions that arise as the spacing decreases and the cylinders no longer behave as independent oscillators.

Figure 7(b) shows the amplitude response as a function of reduced velocity for $0 < G/D < 2$, illustrating how the system transitions into a regime dominated by strong wake coupling. While the amplitude–velocity curves illustrate the overall response trends, the effect of spacing becomes clearer when the peak vibration amplitude is considered directly. Figure 8(a) presents the peak amplitude ratio A^*_{peak} plotted against the gap ratio G/D, highlighting how the maximum response changes with inter-cylinder spacing.

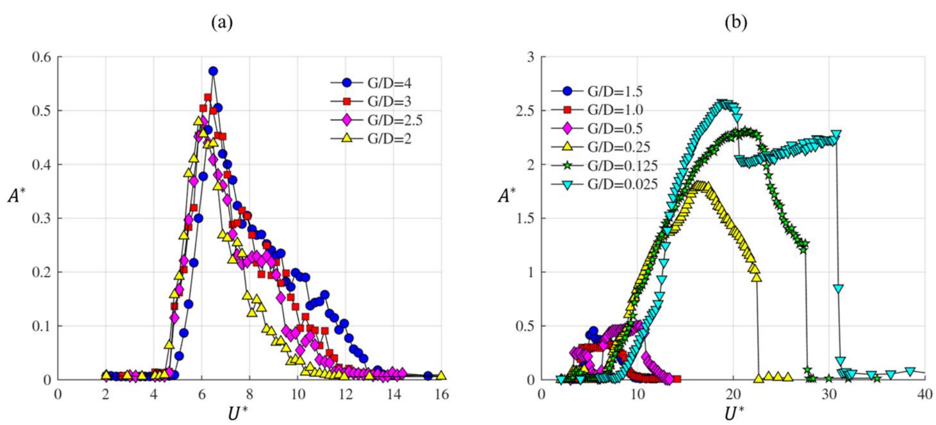

FIG. 7. Amplitude ratio vs reduced velocity for three cylinders arranged side by side (the results correspond to the middle cylinder): (a) $2 \leq \frac{G}{D} \leq 4$ and (b) $0 < \frac{G}{D} < 2$.

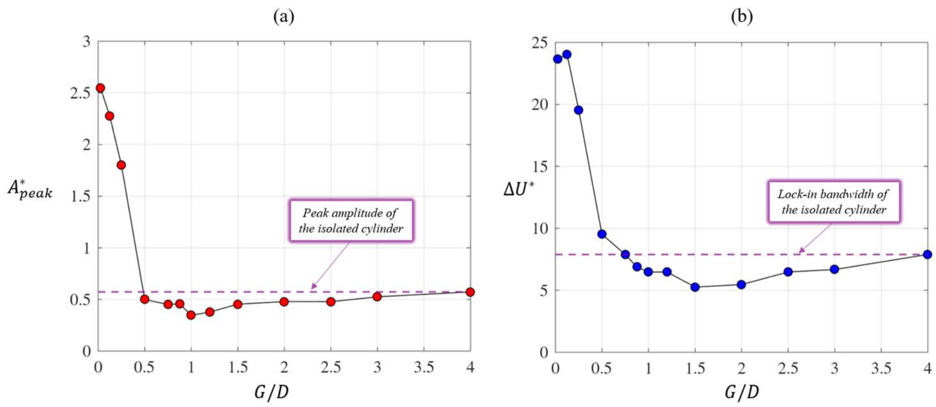

FIG. 8. (a) Peak amplitude ratio A^*_{peak} and (b) lock-in bandwidth ΔU^*, as functions of gap ratio G/D for three cylinders arranged side by side.

As the spacing decreases from $G/D = 4$ to $G/D = 2$, in which the cylinders behave almost independently, the peak amplitude decreases slightly, i.e., from $A^*_{\mathrm{peak}} = 0.60$ to $A^*_{\mathrm{peak}} = 0.48$. This trend mirrors the behavior observed in the two-cylinder array, reflecting mild hydrodynamic interference without substantial modification of the system's vibration capacity.

The peak amplitude remains below the isolated-cylinder value down to $G/D = 0.5$. Although several coupled vibration modes begin to appear within this portion of the interaction range, they do not yet produce an enhancement in the energy transferred from the flow to the structure.

A pronounced change occurs for smaller spacings (G/D 0.5). In this region, the array begins to exhibit significantly larger vibration amplitudes compared to the single-cylinder case. The strongest response is obtained at the smallest spacing tested (G/D 0.025), where the peak response occurs in the in-phase vibration mode. In this state, all three cylinders oscillate synchronously and exhibit similar peak amplitudes, with $A_{\mathrm{peak}} \approx 2.55$, representing more than a fourfold increase relative to isolated-cylinder behavior.

Beyond the peak amplitude trends, the role of spacing in shaping the three-cylinder response is most evident when considering the span of the lock-in region. Because the central cylinder interacts with wakes on both sides, even small changes in G/D can produce pronounced shifts in the onset and cessation of oscillation. Figure 8(b) shows how the lock-in bandwidth ΔU^* evolves across the full range of tested spacings.

The results show that the three-cylinder array begins to exhibit a noticeably wider lock-in range once the spacing is reduced below $G/D = 0.75$. For $0.5 \leq G/D \leq 0.75$, the increase in bandwidth is driven primarily by a reduction in the reduced velocity at which oscillations begin, relative to the single-cylinder case, while the cessation of vibration still occurs at slightly lower velocities than in the isolated-cylinder configuration.

A more dramatic bandwidth expansion occurs for $G/D \leq 0.5$. In this region, the widening is governed mainly by an increase in the reduced velocity at which oscillations cease. For gap ratios smaller than $G/D = 0.125$, the array attains its maximum measured bandwidth of $\Delta U^* = 24$, approximately three times larger than that of a single-cylinder oscillator. This substantial enlargement of the lock-in interval reflects the strong hydrodynamic coupling and enhanced wake coherence that develop at very small gaps, allowing sustained fluid–structure interaction over an extended velocity range.

The trends in amplitude and bandwidth discussed above indicate that the behavior of the three-cylinder array changes qualitatively as the spacing is reduced. For $G/D \geq 2$, the cylinders vibrate in an isolated-like manner and spacing produces only gradual adjustments to onset, cessation, and amplitude. However, once the gap becomes sufficiently small, wake interference intensifies and the system no longer behaves as three independent oscillators. Instead, it enters a strong-interaction regime in which distinct, spacing-dependent vibration modes emerge. These modes are consistent with increasingly complex wake interactions as the center cylinder is coupled to both neighboring cylinders.

As the cylinders are brought closer together, four characteristic oscillation patterns were observed across the lock-in regime:

- *Split-phase mode* (sides in-phase, middle anti-phase) [Fig. 9(a)]. The two outer cylinders oscillate synchronously, while the central cylinder vibrates 180° out of phase with them. This symmetric motion indicates strong coupling and alternating forcing on the middle cylinder from the wakes on either side.
- *Middle-node mode* (sides anti-phase, middle nearly stationary) [Fig. 9(b)]. The outer cylinders oscillate in the opposite phase, whereas the central cylinder remains nearly motionless, exhibiting only small residual fluctuations. The middle cylinder effectively forms a vibration node, dividing the flow into two opposing shear-layer interactions.
- *In-phase mode* [Fig. 9(c)]. At higher reduced velocities, all three cylinders oscillate synchronously with negligible phase differences. This fully coupled state corresponds to a coherent vortex-shedding pattern and produces strong, periodic forcing on the array.
- *Phase-wandering (or collision) mode*. In this unsteady regime, the relative phase between cylinders does not settle into a repeatable phase-locked state. The oscillators exhibit irregular relative motion and may experience intermittent contact, preventing the system from reaching a statistically stationary vibration response over the available measurement interval. For this reason, this regime is identified phenomenologically from the measured displacement signals and visual observations and is treated as an unsteady transitional regime rather than a distinct stable vibration mode.

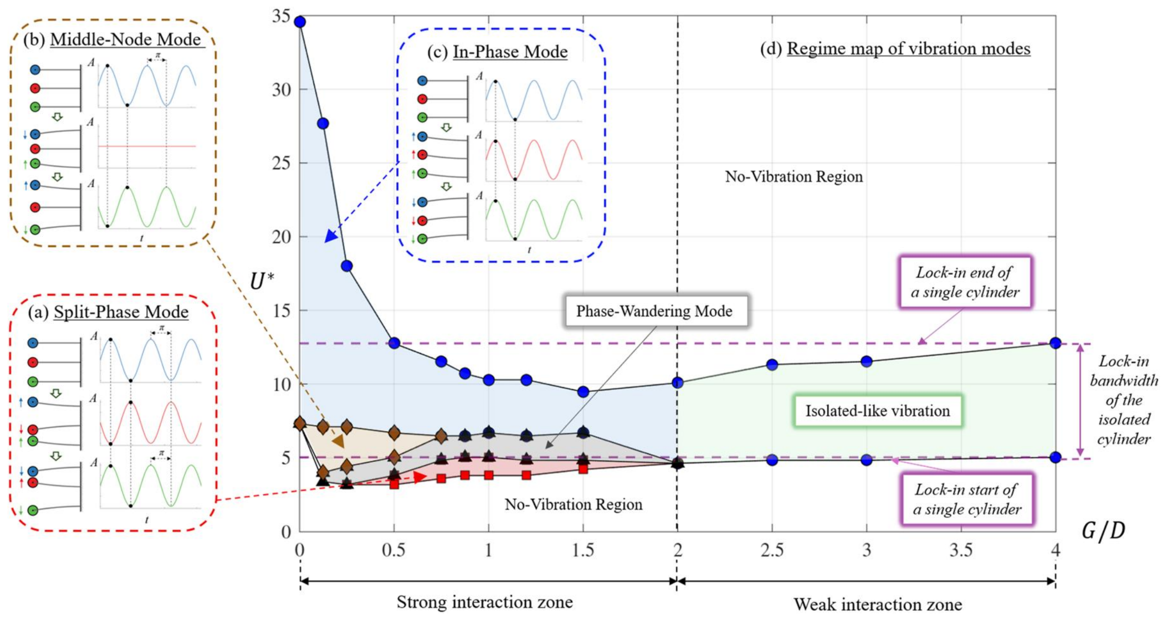

FIG. 9. Vibration modes and regime map for three side-by-side circular cylinders within the strong-interaction regime: (a) split-phase mode (outer cylinders in-phase, middle cylinder in anti-phase); (b) middle-node mode (outer cylinders in anti-phase, middle cylinder stationary); (c) in-phase mode (all cylinders oscillating synchronously); and (d) regime map showing the occurrence of vibration modes.

These behaviors are summarized in the vibration-mode map shown in Fig. 9(d), which compiles the modal structure across all tested spacings and reduced velocities. The map illustrates how the system evolves from isolated-like behavior at large gaps to strongly synchronized motion at very small gaps, providing a clear framework for interpreting how hydrodynamic coupling shapes the response.

The vibration map also reveals clear trends in the onset, progression, and cessation of oscillation. As G/D decreases, the onset of motion shifts to lower reduced velocities, primarily because the split-phase mode becomes active at much smaller U^* values. This mode persists up to the velocity corresponding to the onset of vibration in the isolated cylinder, after which the system transitions into the phase-wandering regime. The unsteady nature of this regime reflects rapid changes in gap-flow topology and the absence of a stable modal structure.

For intermediate spacings $0.75 \leq G/D < 2$, increasing U^* leads to a transition from split-phase or phase-wandering behavior into a stable in-phase mode. This synchronized state persists until the end of the lock-in regime and is associated with coherent vortex shedding and constructive wake interaction.

When the spacing is reduced below $G/D = 0.75$, an additional mode appears, i.e., the middle-node mode, in which the center cylinder remains nearly stationary while the outer cylinders oscillate in anti-phase. Although the motion is constrained by the narrow gaps, further increases in U^* again lead to a transition into the fully synchronized in-phase mode.

Representative amplitude responses of all three cylinders are provided in the supplementary material as Fig. S3. Figure S3(a) shows the case $G/D = 0.25$, where phase-wandering, middle-node, and in-phase regimes are observed as the reduced velocity increases. Figure S3(b) shows the case $G/D = 0.5$, which additionally includes the split-phase mode. These cases illustrate how the amplitudes of the middle and side cylinders evolve across the principal three-cylinder vibration regimes.

A particularly notable finding is that the transition to in-phase motion occurs within a narrow and nearly constant band of reduced velocity, $U^* = 6.7$–7.0, for all spacings from $G/D = 1.5$ down to the smallest tested gap. This consistency indicates that, within the present experimental conditions, the transition to fully coupled in-phase oscillation occurs over a narrow range of reduced velocity. At smaller spacings, oscillations may initiate at lower U^* in split-phase, phase-wandering, or middle-node states; however, the stable in-phase response emerges only after the flow speed is increased further to this narrow transition band. This suggests that the onset of vibration and the onset of fully synchronized in-phase motion are governed by different stages of the coupled wake-oscillator interaction.

The three-cylinder experiments demonstrate that reducing the gap ratio produces substantial amplification of the VIV response. While the array behaves similarly to an isolated oscillator at larger spacings, progressively smaller gaps lead to markedly higher vibration amplitudes—culminating in a peak value of $A^*_{\mathrm{peak}} = 2.55$ at $G/D = 0.025$, more than four times that of the single-cylinder case. The lock-in bandwidth expands in a similar manner: for the smallest spacings, the synchronization range reaches $\Delta U^* = 24$, roughly triple that of an isolated cylinder. These enhancements arise from the emergence of strong hydrodynamic coupling and a sequence of coupled vibration modes that fundamentally reshape the system's dynamic response.

The structural responses observed in both the two- and three-cylinder arrays, particularly the appearance of distinct interaction regimes and spacing-dependent mode transitions, indicate that the underlying wake dynamics change substantially as G/D varies. To identify the aerodynamic mechanisms responsible for these behaviors, qualitative flow-visualization experiments were carried out for both configurations. Section IV C examines how wake topology, gap flow, and vortex-shedding patterns evolve with spacing, providing physical insight into the origins of the vibration modes and their influence on the overall system dynamics.

C. Cylinder wake flow visualization analysis

To complement the vibration measurements and clarify the mechanisms underlying the observed interaction regimes, qualitative flow visualization was conducted for selected configurations of both the two-cylinder pairs and three-cylinder arrays. The objective was to directly observe how the wake structure evolves with decreasing gap ratio and how these changes relate to the transition between different interaction modes. The focus of this analysis was on visualizing the wake patterns associated with the stable and repeatable vibration modes, such as opposite-phase, in-phase, split-phase, and middle-node motion, and relating these structures to the observed variations in vibration amplitude and bandwidth. Representative high-speed flow-visualization videos corresponding to selected vibration modes and wake patterns are provided in the supplementary material.

The flow-visualization images were recorded near the mid-span of the cylinders. The camera was positioned above the model and shifted slightly downstream to capture the near-wake region; therefore, the images correspond to an upper oblique view rather than a perfectly normal top view. In the annotated images, solid white outlines indicate the cylinder boundaries, dashed white lines indicate the cantilever support beams, and colored lines are added as visual guides to highlight the observed vortical structures.

In the pre-lock-in regime, where structural motion is negligible, the wake dynamics are governed primarily by the flow arrangement and cylinder geometry. To establish a baseline for comparison, we first consider the wake behind an isolated cylinder energy harvester mounted on a flexible beam,[9] as shown in the supplementary material [Fig. S4(a)]. In this configuration, no periodic vortex formation was observed during pre-lock-in. A later investigation by Fershalov *et al.*[44] demonstrated that this absence of vortex shedding is linked to the flexibility of the support beams and the finite aspect ratio of the cylinder, both of which can suppress or delay the roll-up of shear layers. This explanation was validated experimentally by mounting the same cylinder on a rigid support, which resulted in clear vortex shedding under identical flow conditions, a behavior not present when the cylinder was attached to flexible beams. Consistent with these findings, pre-lock-in flow visualization for the two- and three-cylinder arrays with the minimum spacing $G/D = 0.025$ also revealed no vortex formation [supplementary material Figs. S4(b) and (c)]. The wake boundaries remained distinct and steady, showing no periodic fluctuations or signs of shear-layer roll-up.

More complex wake features appeared at moderate gap ratios $(0.025\ G/D\ 0.5)$. For the two-cylinder configuration, the gap flow exhibited a distinct bias toward one side [supplementary material Fig. S5(a)], even though no organized vortices were yet present. In the three-cylinder array, each gap flow was biased toward its respective outer cylinder [supplementary material Fig. S5(b)], producing an asymmetric wake with unequal shear-layer development on the two sides.

In the strong-interaction zone $(G/D \leq 1)$, once the reduced velocity increases beyond the pre-lock-in regime, the two-cylinder array first enters the anti-phase vibration mode [Fig. 6(a)]. In this mode, the cylinders move symmetrically in opposite directions, and the wake structure evolves in a repeatable sequence over each oscillation cycle. When the cylinders diverge from one another, two synchronized and symmetric vortices form on the outer sides of the cylinders, where the shear layers roll up cleanly due to the unobstructed cross-flow.

As the cylinders approach their maximum separation and begin to the reverse direction, a gap vortex starts to develop between them. This vortex exhibits a characteristic mushroom-shaped structure, consisting of two counter-rotating shear-layer motions induced by the instantaneous constriction and redirection of the gap flow. When the cylinders move toward each other and the gap reaches its minimum width, the developing gap vortex is pushed downstream and expelled from between the cylinders. As this vortex convects further downstream, it merges into a single coherent structure.

A notable feature of the gap vortex is its systematic bias toward the lower cylinder. After being expelled, the vortex is consistently deflected downward and eventually merges with the outer vortex on the lower side. This bias is attributed to slight asymmetries in the instantaneous pressure distribution and gap-flow geometry during the cylinder motion, despite the nominal geometric symmetry of the setup. Such directional bias in the gap vortex is commonly reported in side-by-side configurations[39–42] and is a precursor to asymmetric wake development at higher reduced velocities.

A sequence of photographs illustrating one complete cycle of the anti-phase vibration mode is presented in Fig. 10, highlighting the formation, advection, and merging of the gap vortex and the outer shear-layer structures.

The split-phase vibration mode is observed in the three-cylinder array within the strong-interaction range $0.25 < G/D < 2$. In this mode, the two outer cylinders oscillate in phase, while the central cylinder moves 180° out of phase with them [Fig. 9(a)]. This arrangement effectively creates two coupled pairs: each outer cylinder interacts with the middle cylinder as an opposite-phase pair, while the outer cylinders maintain synchronous motion with one another. As a result, the wake generated in this mode is considerably more complex than that of the two-cylinder configuration.

During the outward motion of the outer cylinders, each generates its own pair of outer-side vortices, formed by the roll-up of the shear layers on the outer faces of the array. Simultaneously, as the cylinders reverse direction and move toward the center, two gap vortices develop (i.e., one in each gap between an outer cylinder and the central one). These gap vortices exhibit a counter-rotating structure, shaped by the compression and redirection of the gap flow as the cylinders approach one another.

Once formed, the gap vortices are convected downstream, where they merge with the nearest outer-side vortex produced by the adjacent outer cylinder. This merging process generates alternating vortex pairing occurring on each cycle.

A sequence of photographs, illustrating one complete cycle of the split-phase vibration mode, is presented in Fig. 11(a), highlighting the formation, evolution, and downstream merging of the gap and outer-side vortices in this strongly coupled three-body system.

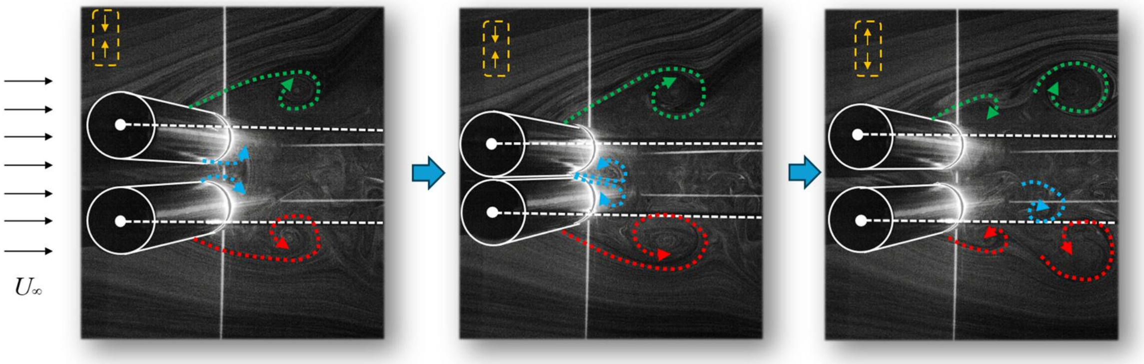

FIG. 10. Chronological sequence of flow-visualization photographs illustrating one representative cycle of the opposite-phase vibration mode for the two-cylinder array at $G/D = 0.25$ and $U^* = 5$. Colored lines highlight the locations and evolution of vortical structures for clarity.

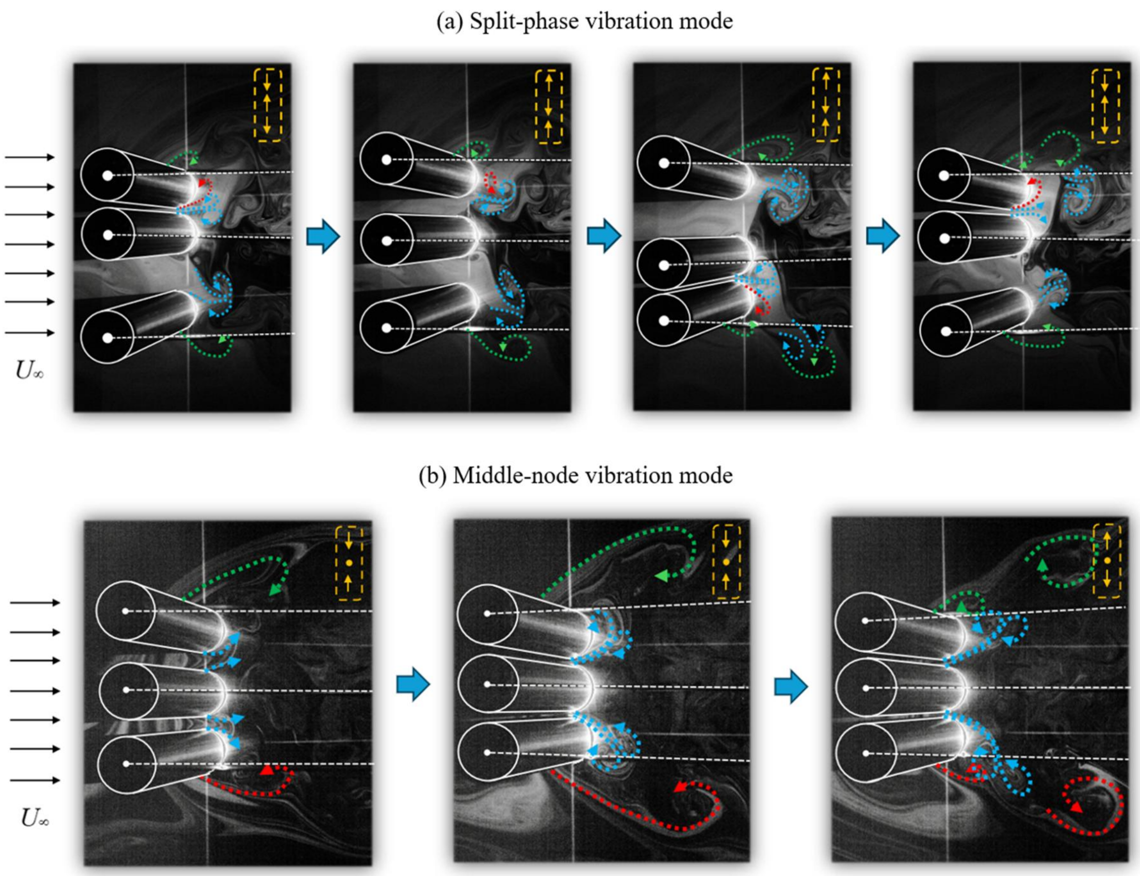

FIG. 11. Sequence of flow-visualization photographs illustrating one complete cycle of vibration for the three-cylinder array: (a) split-phase vibration mode for the three-cylinder array at $G/D = 0.5$ and $U^* = 3.5$ and (b) middle-node vibration mode in the three-cylinder array at $G/D = 0.25$ and $U^* = 5.5$. Colored lines highlight the locations and evolution of vortical structures for clarity.

Within the strong-interaction range $0.025 < G/D < 0.75$, the three-cylinder array can exhibit the middle-node vibration mode. In this mode, the central cylinder remains nearly stationary while the two outer cylinders oscillate in the opposite phase [Fig. 11(b)]. Because the middle cylinder acts as a kinematic node, the wake is shaped entirely by the motion of the outer cylinders.

When the outer cylinders move apart, the shear layers on their outer sides roll up into a pair of symmetric vortices similar to those observed in the two-cylinder opposite-phase mode. As the cylinders reverse direction and move toward the middle cylinder, two mushroom-shaped gap vortices form—one in each gap. These vortices are produced by the rapid convergence of the gap flow and the associated compression of the shear layers between each outer cylinder and the stationary center body.

Once formed, the gap vortices are convected downstream, where they merge with the vortices shed from the inner sides of the outer cylinders. Each gap vortex is deflected slightly outward as it travels, eventually merging with the outer vortex of the corresponding outer cylinder. This pairing process results in a wake structure that is symmetric but more intricate than that of the two-cylinder opposite-phase case, due to the presence of two interacting gap regions anchored by a stationary central body.

A series of photographs illustrating one full cycle of the middle-node vibration mode is shown in Fig. 11(b), capturing the formation, evolution, and downstream merging of the gap vortices in this strongly coupled three-body configuration.

As the reduced velocity increases within the strong-interaction zone ($0.025 \leq G/D < 2$), all configurations, regardless of spacing or array size, ultimately converge to a stable in-phase vibration mode. This transition consistently marks the point at which the wake becomes fully synchronized across cylinders, enabling sustained, large-amplitude oscillations. Because the wake behavior is qualitatively similar for both the two- and three-cylinder arrays at the smallest spacing, the three-cylinder configuration is used here to illustrate the wake evolution in this regime.

The wake modes are described using the standard VIV notation:[3,5,8] 2S denotes two single vortices shed per oscillation cycle, with one vortex shed during each half-cycle of motion, whereas 2P denotes two vortex pairs shed per oscillation cycle, with one pair formed during each half-cycle.

For the minimum gap case ($G/D = 0.025$), the three-cylinder array remained in the in-phase mode throughout the lock-in range. During the initial branch, flow visualization revealed a well-organized 2S vortex-shedding mode, characterized by the alternate shedding of single vortices from each side of the outer shear layers during successive half-cycles. The wake was highly symmetric, indicating strong aerodynamic coupling among all three cylinders. A sequence of photographs at $U^* = 11$ and $A^* = 0.5$, showing one full vibration cycle and the corresponding vortex evolution, is presented in Fig. 12(a).

As the flow velocity increased, the vibration amplitude grew steadily while the wake continued to exhibit a 2S shedding mode up to the peak response. During this stage, the vortices formed closer to the cylinder surfaces and exhibited larger cores, reflecting intensified fluid–structure coupling. A series of photographs near the peak-amplitude condition ($U^* = 19$, $A^* = 2.5$) is shown in Fig. 12(b), illustrating the evolution of the wake over a complete oscillation cycle.

After the peak response, the amplitude dropped abruptly to approximately $A^* = 2.0$ at $U^* \approx 21$. Following this transition, the wake shifted from a 2S to a 2P vortex-shedding mode, in which pairs of vortices were shed from each side during each half-cycle of motion. This structural change in the wake topology is documented in Fig. 12(c), captured at $U^* = 22$ and $A^* = 2.0$.

The observed transition from 2S to 2P shedding at higher reduced velocities is consistent with trends widely reported for single-cylinder VIV systems.[3,5,8,9,44] Notably, the multi-cylinder arrays exhibit the same qualitative behavior, indicating that the underlying flow-structure mechanisms governing the shedding transition remain fundamentally similar even in the presence of strong multi-body wake coupling.

For the moderate spacing case $G/D = 0.25$, the three-cylinder array exhibits additional wake features during the in-phase vibration regime ($U^* > 7$). At low vibration amplitudes, flow visualization shows that gap vortices form during each half cycle of oscillation, much like the vortices shed from the outer sides of the cylinders. Because all three cylinders move synchronously, the instantaneous gap geometry is the same on both sides, and the vortices generated in the gaps are nearly symmetric in size and timing.

During each half cycle, the two gap vortices are drawn toward and entrained into the outer-side vortex located opposite to the direction of cylinder motion. This merging process reflects the strong, coherent shear-layer interaction that develops when all cylinders accelerate in the same direction, causing the gap shear layers to roll up and convect toward the dominant outer vortex. The consistent pairing of gap vortices with the corresponding outer vortices produces a well-organized wake despite the presence of multiple interacting shear layers.

A sequence of photographs captured at $U^* = 8$ and $A^* = 0.4$, illustrating one full cycle of this behavior, is presented in Fig. 13(a).

As the vibration amplitude increases with rising U^*, the gap vortices become progressively less distinct. At large pre-peak amplitudes, such as those observed at $U^* = 15.5$, the flow through the gaps no longer rolls up into clearly identifiable vortex structures. Instead, the gap shear layers merge directly with the large outer vortex formed downstream of the array, producing an even larger, more coherent structure. Despite this change in vortex organization, the wake maintains a 2S shedding mode, with a single dominant vortex generated on each side during every half cycle of motion. A series of photographs captured at $U^* = 15.5$ and $A^* = 1.7$, illustrating this behavior, is presented in Fig. 13(b).

After passing the peak vibration amplitude, the wake structure undergoes a transition to a 2P shedding pattern, similar to that observed for the smallest-gap configuration [see Fig. 12(c)]. In this regime, pairs of vortices are shed from each side during every half-cycle of motion.

In the post-lock-in regime, no periodic vortex structures were observed for any configuration. Instead, the wake became irregular and non-shedding, consistent with the loss of organized fluid–structure synchronization. For moderate gap ratios, however, a biased wake pattern was still present, similar to that seen in the pre-lock-in regime.

Examples of this asymmetric wake behavior at moderate spacing (G/D 0.25) are shown in the supplementary material (Fig. S6). For the two-cylinder array at $U^* = 17$ [supplementary material Fig. S6(a)], the wake is consistently biased toward the lower cylinder. In the three-cylinder array at $U^* = 24$ [supplementary material Fig. S6(b)], the bias manifests differently: the middle cylinder's wake is deflected upward toward the upper outer cylinder. These post-lock-in asymmetries reflect residual interactions between the gap flow and the outer shear layers, even after the cessation of periodic vortex shedding.

The flow-visualization results provide valuable qualitative insight into how wake dynamics shape the vibration behavior of two- and

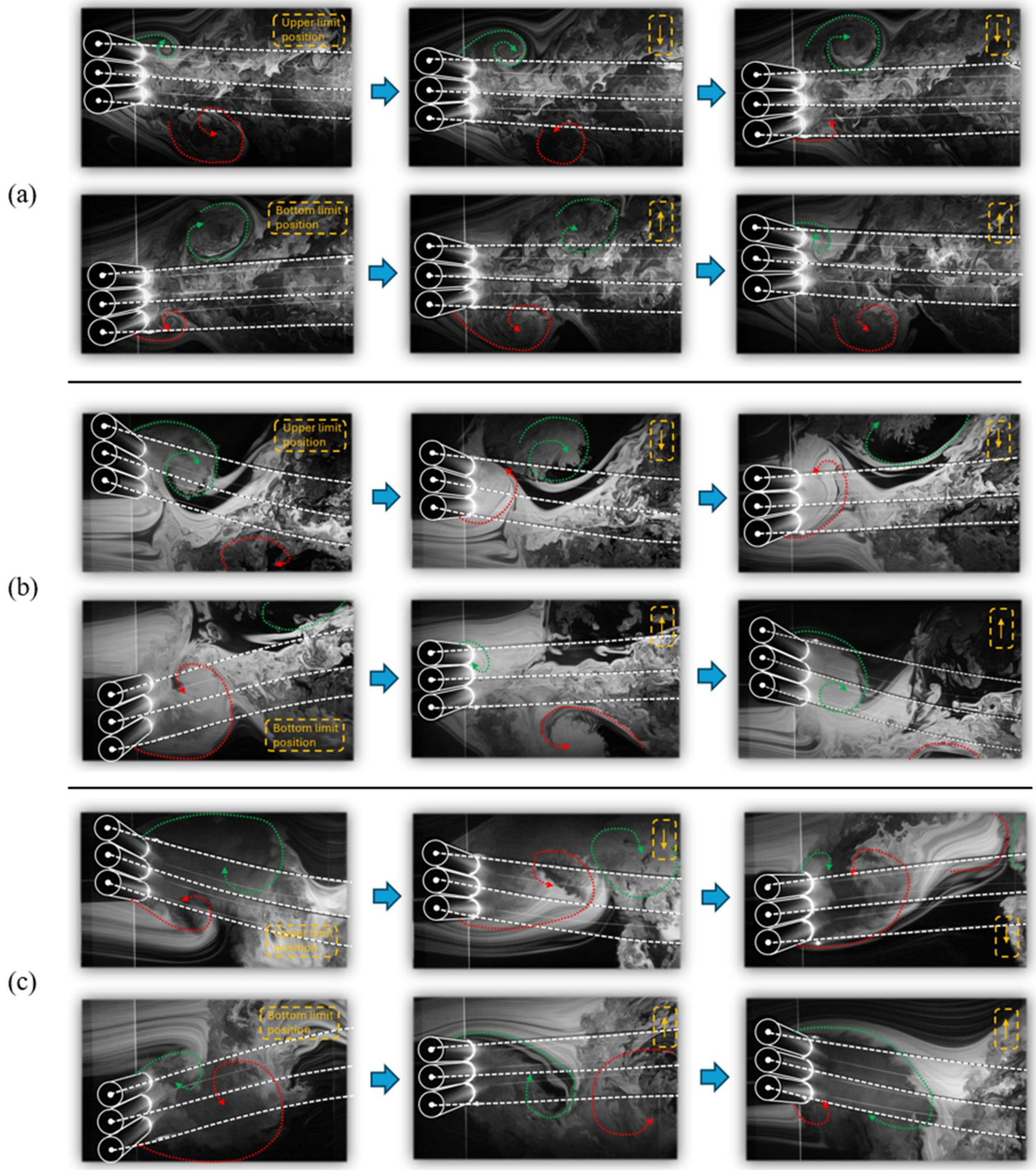

FIG. 12. Flow-visualization photographs showing one complete cycle of the in-phase vibration mode for the three-cylinder array ($G/D = 0.025$): (a) $U^* = 11$, $A^* = 0.5$; (b) $U^* = 19$, $A^* = 2.5$; and (c) $U^* = 22$, $A^* = 2.0$. Colored lines highlight the locations and evolution of vortical structures for clarity.

three-cylinder arrays. Observations across the pre-lock-in, lock-in, and post-lock-in regimes clarify when and how organized vortex shedding emerges, how distinct wake topologies correspond to specific vibration modes, and why certain configurations produce amplified responses or broadened lock-in ranges. In particular, the visualization helps link mode transitions, such as opposite-phase, split-phase, middle-node, and in-phase motion, to changes in gap-flow behavior and vortex formation. In the post-lock-in regime, the disappearance of periodic shedding and the persistence of biased but irregular wake structures further illustrate how aerodynamic coupling weakens as oscillations decay. Overall, wake observations serve as a physical framework for interpreting the measured vibration responses

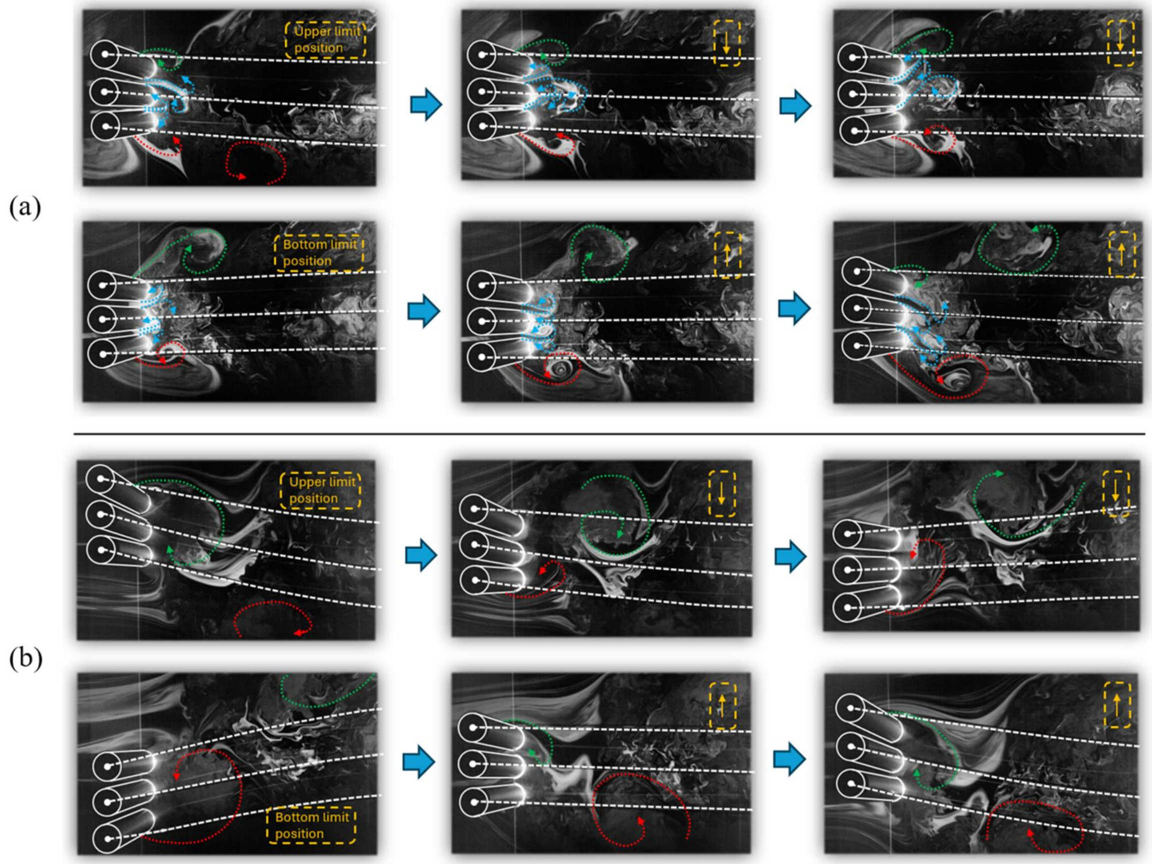

FIG. 13. Flow-visualization photographs showing one complete cycle of the in-phase vibration mode for the three-cylinder array at $G/D = 0.25$: (a) $U^* = 8$, $A^* = 0.4$ and (b) $U^* = 15.5$, $A^* = 1.7$. Colored lines highlight the locations and evolution of vortical structures for clarity.

and for understanding the fluid–structure mechanisms that govern multi-cylinder VIV behavior.

D. Energy harvesting analysis

The flow-visualization results discussed above show that the largest vibration amplitudes occur when the arrays reach coherent in-phase lock-in states, where organized vortex shedding and strong wake coupling sustain large-amplitude motion over an extended velocity range. The energy-harvesting potential of the cylinder arrays is, therefore, estimated using the optimal piezoelectric power model introduced in Sec. II and applied to the isolated-cylinder harvester in Ref. 9. Because this model scales with A^{*2}, the wake-coupled regimes that produce the largest and most sustained mechanical response also correspond to the highest estimated harvesting potential. Under the standard resistive-load formulation and the weak electromechanical coupling assumption, the nondimensional optimal power reduces to the simple expression, i.e., $P^*_{\mathrm{piezo,opt}} = \frac{1}{2}(A^*)^2$, valid throughout the lock-in regime where $\omega \approx \omega_n$. This expression shows that the harvested power depends solely on the square of the dimensionless vibration amplitude. Consequently, the significant amplification of A^* observed at small gap ratios, together with the substantial widening of the lock-in bandwidth, directly enhances the potential energy output of the multi-cylinder arrays.

To quantify these effects, the peak vibration amplitudes A^*_{peak} from the single-cylinder configuration and from the array cases are plotted together as a function of the mass-damping parameter $m^*\zeta$ [Fig. 14(a)]. For the two- and three-cylinder arrays, only the gap ratios that produced amplified amplitudes relative to the isolated cylinder are included in this comparison.

Using the same amplitude data, the optimal nondimensional power is computed for the selected G/D configurations that exhibited amplified responses. These power estimates [Fig. 14(b)] are displayed alongside the vibration data on the A^*-$m^*\zeta$ plot, allowing direct comparison of the energy-harvesting potential across the single-, two-, and three-cylinder cases. The peak-response conditions used in this comparison occur in the in-phase vibration regime, where all cylinders oscillate at the same dominant frequency, close to the measured natural frequency $f_n = 2.44$ Hz. Therefore, the reported power enhancements are per-oscillator estimates.

These comparisons highlight the strong enhancement in energy-harvesting performance achieved through aerodynamic coupling, especially for tightly spaced arrays that exhibit large amplitude growth and extended lock-in ranges.

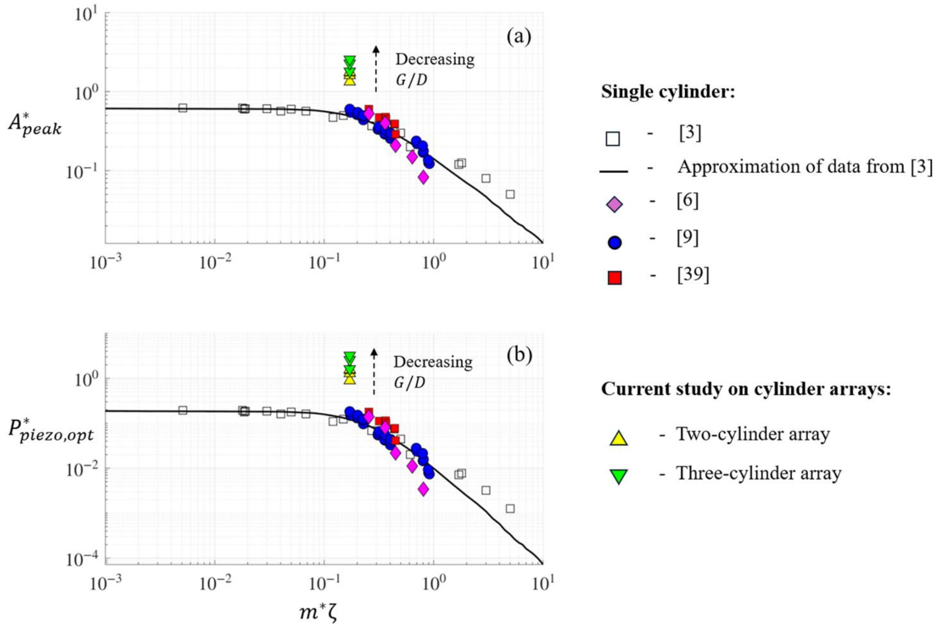

FIG. 14. Effect of mass-damping ratio on (a) peak amplitude ratio and (b) optimal dimensionless harvested power at peak vibration.

An important consideration for flow-energy harvesting is not only the magnitude of the peak vibration amplitude A^*_{peak} but also the reduced velocity at which this peak occurs. The Skop–Griffin parameter, SG, provides a convenient way to organize the peak-amplitude data by combining the effects of mass ratio, damping, and reduced velocity into a single nondimensional group. For a given structural configuration (m^*, ζ), varying the flow speed changes SG essentially through U^*, so that lower values of SG correspond to operation at higher reduced velocities.

Figure 15 presents the peak-amplitude data plotted in the $A^* - SG$ plane for the isolated cylinder and for those two- and three-cylinder configurations that displayed amplified responses. As expected, the single-cylinder measurements follow the classical trend of decreasing A^*_{peak} with increasing SG, consistent with previously reported VIV amplitude correlations.[3,6,9,44] The multi-cylinder datasets cluster in a distinctly different region of the plot: they reach substantially larger peak amplitudes while operating at lower values of SG. This shift arises because the arrays attain their maximum response at significantly higher reduced velocities than the single-cylinder oscillator.

Although closely spaced cylinder arrays achieve substantially larger vibration amplitudes than the isolated cylinder, this amplification does not indicate improved energy-conversion efficiency at a fixed reduced velocity. Instead, the arrays reach their peak responses at higher values of U^*, where a greater amount of flow-induced forcing is available to sustain large oscillations. The increased amplitude, therefore, reflects operation at a different part of the velocity spectrum, not a more efficient transfer of energy from the flow to the structure.

This distinction becomes apparent when comparing responses at the same reduced velocity. The isolated cylinder reaches its peak amplitude of $A^* = 0.6$ at $U^* = 6.3$. In contrast, the tightly spaced

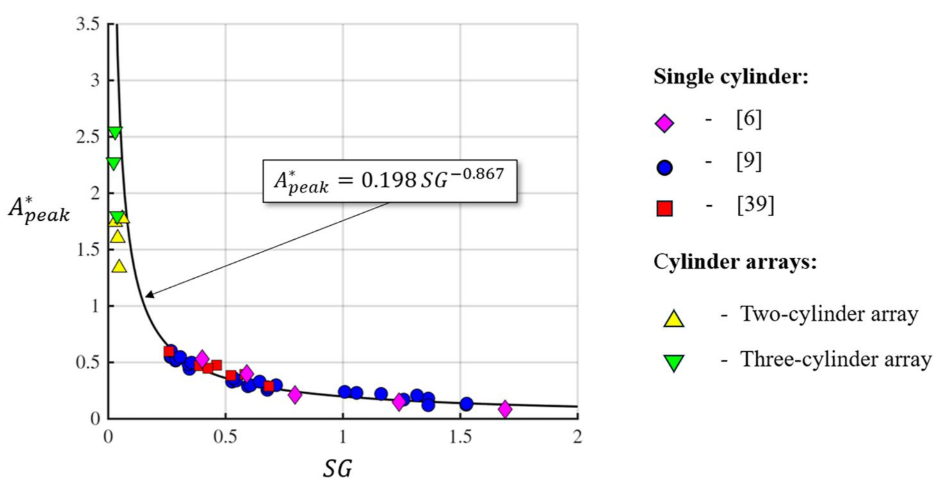

FIG. 15. Peak dimensionless amplitude A^*_{peak} plotted against the Skop–Griffin parameter.

two- and three-cylinder arrays ($G/D = 0.025$) exhibit almost no vibration at this same U^*, despite producing very large amplitudes at higher velocities. Thus, the closely spaced arrays have a higher effective cut-in reduced velocity for the amplified coupled response and may perform poorly at very low flow speeds if the system is not tuned to the intended operating range. For the closely spaced configurations that eventually exceed the isolated-cylinder amplitude (G/D 0.25), this crossover occurs approximately at $U^* \approx 7.5 - 9$ for the two-cylinder array and $U^* \approx 9 - 11$ for the three-cylinder array, depending on the gap ratio. This illustrates that while close spacing can yield dramatic increases in the harvested power, the benefit depends strongly on where the amplified response occurs relative to the available operating flow speed. For energy-harvesting applications, the effectiveness of a given spacing is, therefore, determined not by the magnitude of the peak response alone, but by whether the amplified vibration occurs within the range of flow velocities expected in the intended operating environment.

A key implication of this analysis is that effective energy-harvester design requires aligning the peak-response reduced velocity with the expected free-stream velocity of the application. Since U^* depends on the free-stream velocity, natural frequency, and cylinder diameter, designers can tune the response by adjusting f_n and D. To achieve large amplitudes at practical flow speeds, the mass should be minimized, since smaller values shift the system toward higher responsiveness and greater vibration amplitudes. Because of this, practical tuning is accomplished by adjusting the natural frequency through modifications to the beam stiffness (via changes in geometry, thickness, or material properties). Selecting an appropriate cylinder diameter provides an additional mechanism for positioning the peak response within the desired U^* range. By jointly tuning f_n and D while keeping the system with a favorable low mass, the harvester can be configured so that the spacing-induced amplification observed in multi-cylinder arrays occurs at flow velocities relevant to the intended environment, thereby enabling meaningful gains in harvested power.

To further examine this relationship, single-cylinder data from Refs. 6, 9, and 44 were combined and fitted with the empirical power law as follows:

$$A^* = 0.198\, SG^{-0.867}. \tag{17}$$

Remarkably, when the present two- and three-cylinder array data are plotted alongside this correlation in Fig. 15, they also collapse well onto the same curve, despite occupying lower SG values due to their higher peak U^*. This collapse indicates that the fundamental amplitude scaling with SG remains unchanged by wake coupling. The arrays do not alter the intrinsic functional dependence of the VIV amplitude on SG; instead, they simply shift the effective operating point into the low-SG, high-A^* regime. From a modeling and design perspective, this suggests that amplitude correlations originally developed for isolated cylinders may be extended to side-by-side arrays, provided that the effective SG value corresponding to the operating U^* is properly accounted for.

In Ref. 9, the power output of the isolated-cylinder harvester was estimated using a piezoelectric patch (PZT-5A) bonded near the clamped end of the cantilever beam. The electromechanical coupling coefficient θ and capacitance C_{piezo} of the patch were obtained from beam-piezo geometry and material properties, and the optimal power under a resistive load was evaluated using $P_{\text{piezo,opt}} = \frac{\omega\theta^2_{\text{piezo}}A^2}{2C_{\text{piezo}}}$, corresponding to Eq. (14) in the present work. For the isolated cylinder configuration with diameter $D = 40$ mm, vibrating mass $m = 70$ g, and maximum displacement $A = 24.1$ mm ($A^* \approx 0.60$), the optimal power output was found to be $P^{\text{single}}_{\text{piezo,opt}} \approx 1.8$ mW.[9]

Since all geometric, structural, and piezoelectric parameters (ω, θ, C_p) remain unchanged in the present study, the optimal power scales quadratically with the vibration amplitude as follows:

$$P^{\text{array}}_{\text{piezo,opt}} = P^{\text{single}}_{\text{piezo,opt}}\left(\frac{A_{\text{array}}}{A_{\text{single}}}\right)^2. \tag{18}$$

For a fixed cylinder diameter D, the dimensional amplitude ratio is identical to the ratio of dimensionless amplitude, so that $P^{\text{array}}_{\text{piezo,opt}} = P^{\text{single}}_{\text{piezo,opt}}\left(\frac{A^*_{\text{array}}}{A^*_{\text{single}}}\right)^2$. Using $A^* = 0.6$ for the isolated cylinder, $P = 1.8$ mW, and the representative per-oscillator peak amplitudes in the in-phase array response, $A^* = 1.77$ for each cylinder in the two-cylinder array at $G/D = 0.025$ and $A^* \approx 2.55$ for each cylinder in the three-cylinder array at $G/D = 0.025$, the corresponding optimal powers per oscillator are 15.7 and 32.5 mW. Since the cylinder span was fixed at $L = 0.4$ m for all configurations, these values correspond to peak optimal powers per unit cylinder length of 4.5 mW/m for the isolated cylinder, 39.3 mW/m for each oscillator in the two-cylinder array, and 81.3 mW/m for each oscillator in the three-cylinder array. Thus, under the same piezoelectric configuration and optimal resistive loading, the two-cylinder and three-cylinder arrays yield substantial increases in power per oscillator relative to the isolated-cylinder case. Because these estimates are based on the vibration amplitude of an individual oscillator, they should be interpreted as per-oscillator enhancements; the total array power would then scale with the number of oscillators equipped with piezoelectric elements.

These estimates indicate the substantial potential gains in power output that could be obtained under the same piezoelectric configuration and optimal resistive loading by exploiting strong wake coupling in closely spaced multi-cylinder arrays.

The power estimates discussed above are based on the response in the in-phase vibration regime, where all cylinders move synchronously and the corresponding piezoelectric voltages are nominally in phase. In this configuration, electrical integration is straightforward: the piezo patches can be connected to a common rectifier or combined in parallel (with consistent poling), allowing their currents to add so that the total harvested power scales directly with the number of oscillators.

For other vibration modes, such as the opposite-phase mode in the two-cylinder array and the split-phase or middle-node modes in the three-cylinder configuration, the mechanical motion of individual cylinders is not phase-aligned. If the raw AC piezoelectric outputs were simply connected together, these phase differences could lead to partial voltage cancelation and a reduction in net power. In practice, this issue can be avoided by treating each oscillator as an independent electrical channel, each with its own rectifier and power-conditioning circuit, or by selecting the wiring polarity so that mechanically out-of-phase motions generate electrically in-phase voltages.

However, the present experiments show that the largest vibration amplitudes and the widest lock-in ranges consistently occur in the in-phase regime for both two- and three-cylinder arrays. From an energy-harvesting perspective, this indicates that practical array designs should aim to promote and stabilize in-phase vibration, using other modes primarily as transitional or secondary states rather than as the desired operating condition.

V. CONCLUSIONS

This study experimentally examined VIV of two- and three-cylinder arrays arranged side by side and mounted on flexible beams, with particular emphasis on how wake coupling and inter-cylinder spacing govern vibration amplitude, lock-in bandwidth, modal behavior, and the underlying fluid–structure interaction mechanisms. The gap-to-diameter ratio G/D was varied from 0.025 to 4, enabling observation of the transition from isolated-cylinder behavior to strongly coupled oscillations.

An isolated single cylinder served as a reference case, exhibiting a peak non-dimensional amplitude of $A^* \approx 0.60$ near $U^* \approx 6.3$, with vibration initiating at $U^* \approx 5$ and ceasing at $U^* \approx 12.5$, corresponding to a lock-in bandwidth of $\Delta U^* \approx 7.5$. For both array configurations, a weak-interaction regime was identified at larger spacings, where the response closely resembled that of the isolated cylinder, with only modest reductions in peak amplitude and gradual shifts in the termination of lock-in as spacing decreased.

At smaller gap ratios, strong hydrodynamic coupling fundamentally altered the VIV response. In the two-cylinder array, strong interaction emerged for $G/D < 1$, accompanied by the appearance of coupled vibration modes and pronounced amplification of both amplitude and lock-in bandwidth. At the smallest spacing tested ($G/D = 0.025$), the peak amplitude reached $A^* = 1.8$, approximately three times the isolated-cylinder value, while the lock-in bandwidth expanded to $\Delta U^* \approx 17$.

The three-cylinder array exhibited strong-interaction effects at even larger spacings ($G/D < 2$), reflecting the central cylinder's simultaneous exposure to wakes from both neighbors. Several distinct coupled vibration modes were observed, illustrating the increased dynamical complexity of the three-body system. At $G/D = 0.025$, the peak amplitude increased to $A^* = 2.55$, more than four times that of the isolated cylinder, and the lock-in bandwidth expanded to $\Delta U^* = 24$, nearly tripling the baseline value.

A notable consequence of strong wake coupling is the substantial broadening of the operational velocity range. Whereas the isolated cylinder exhibits large-amplitude oscillations only within a narrow interval near its peak response, the two-cylinder array sustains amplitudes exceeding the isolated-cylinder maximum over $9 \leq U^* \leq 21$, and the three-cylinder array over an even wider range, $12 \leq U^* \leq 31$. This marked expansion of the lock-in regime highlights the role of collective wake dynamics in maintaining synchronized forcing over a broad range of flow conditions.

Flow-visualization experiments provided physical insight into these behaviors, revealing mode-dependent wake structures during lock-in and the absence of coherent periodic vortex shedding in both pre- and post-lock-in regimes, consistent with the effects of structural flexibility and finite cylinder length.

Using a previously validated piezoelectric power model, the amplified vibration responses were shown to correspond to substantially higher potential energy extraction per oscillator relative to the isolated-cylinder case. However, the peak responses of the arrays occurred at progressively higher reduced velocities, indicating that strong wake coupling does not inherently increase harvesting efficiency but rather shifts the amplified-response regime to higher flow speeds. Realizing these large-amplitude states, therefore, requires that the structural natural frequency be matched to the flow conditions so that the operational velocity coincides with the amplified-response region in reduced-velocity space.

The strongest vibration amplitudes and widest lock-in bandwidths were consistently associated with fully synchronized, in-phase oscillation, whereas out-of-phase modes were confined to the onset of lock-in and produced weaker responses. This highlights the importance of vibration-mode selection for practical applications, particularly for energy-harvesting systems where synchronized motion is also advantageous for electrical power combination.

Overall, this study demonstrates that controlled wake coupling in side-by-side cylinder arrays fundamentally alters the vortex-structure interaction, enabling access to large-amplitude, wide-bandwidth VIV responses when the system is appropriately tuned. These findings provide physical insight into collective wake dynamics in multi-body systems and offer guidance for the development of multi-oscillator VIV energy harvesters, while also establishing a foundation for future experimental and numerical investigations of coupled fluid–structure interactions.

The present findings may also be relevant to broader engineering systems containing multiple cylindrical or wire-like elements exposed to cross-flow. Examples include tube banks, cable arrays, sensor supports, and wire-electrode arrangements, where spacing-dependent wake interference can influence unsteady aerodynamic loading, vibration levels, and long-term structural reliability. The observed sensitivity of vibration amplitude, lock-in bandwidth, and synchronization mode to inter-cylinder spacing highlights the importance of geometric arrangement when designing cylindrical arrays subjected to flow-induced excitation.

SUPPLEMENTARY MATERIAL

See the supplementary material for the supporting experimental results and flow-visualization images. It includes the isolated-cylinder amplitude response used as the baseline for comparison with the two- and three-cylinder arrays, a schematic of the wind tunnel facility and experimental arrangement, and representative amplitude–response curves for the individual cylinders in selected three-cylinder configurations. It also includes flow-visualization images showing pre- and post-lock-in wake behavior for isolated, two-cylinder, and three-cylinder cases at selected gap ratios. These materials provide additional context for the vibration responses, mode transitions, and wake-interaction mechanisms discussed in the main text.

ACKNOWLEDGMENTS

This research work was supported by the National Science Foundation (NSF) Award No. 2131600 and the Professional Staff Congress-City University of New York (PSC-CUNY) Enhanced Award.

AUTHOR DECLARATIONS

Conflict of Interest

The authors have no conflicts to disclose.

Author Contributions

Andrei Fershalov: Conceptualization (equal); Data curation (lead); Formal analysis (lead); Investigation (lead); Methodology (equal); Validation (lead); Visualization (lead); Writing – original draft (lead); Writing – review & editing (equal). **Niell Elvin:** Conceptualization (equal); Data curation (equal); Formal analysis (equal); Funding acquisition (equal); Investigation (equal); Methodology (equal); Project administration (equal); Resources (equal); Supervision (equal); Validation (equal); Visualization (equal); Writing – original draft (equal); Writing – review & editing (equal). **Mikhail Fershalov:** Data curation (equal); Formal analysis (equal); Investigation (equal); Visualization (equal). **Daniel Struk:** Data curation (equal); Investigation (equal); Visualization (equal). **Yang Liu:** Conceptualization (equal); Formal analysis (equal); Funding acquisition (equal); Investigation (equal); Methodology (equal); Project administration (equal); Resources (equal); Software (equal); Supervision (equal); Visualization (equal); Writing – review & editing (equal).

DATA AVAILABILITY

The data that support the findings of this study are available from the corresponding author upon reasonable request.

REFERENCES

[1] P. W. Bearman, "Vortex shedding from oscillating bluff bodies," Annu. Rev. Fluid Mech. **16**, 195–222 (1984).
[2] T. Sarpkaya, "A critical review of the intrinsic nature of vortex-induced vibrations," J. Fluids Struct. **19**(4), 389–447 (2004).
[3] C. H. K. Williamson and R. Govardhan, "Vortex-induced vibrations," Annu. Rev. Fluid Mech. **36**, 413–455 (2004).
[4] A. Khalak and C. H. K. Williamson, "Investigation of the relative effects of mass and damping in vortex-induced vibration of a circular cylinder," J. Wind Eng. Ind. Aerodyn. **69–71**, 341–350 (1997).
[5] A. Khalak and C. H. K. Williamson, "Motions, forces and mode transitions in vortex induced vibrations at low mass-damping," J. Fluids Struct. **13**, 813–851 (1999).
[6] C. Feng, "The measurement of vortex induced effects in flow past stationary and oscillating circular and d-section cylinders," Ph.D. dissertation (University British Columbia, Vancouver, Canada, 1968).
[7] P. Anagnostopoulos and P. W. Bearman, "Response characteristics of a vortex-excited cylinder at low Reynolds numbers," J. Fluids Struct. **6**(1), 39–50 (1992).
[8] R. Govardhan and C. H. K. Williamson, "Modes of vortex formation and frequency response for a freely-vibrating cylinder," J. Fluid Mech. **420**, 85–130 (2000).
[9] A. Fershalov, N. Elvin, P. Orlandini, I. Avros, and Y. Liu, "Harvesting sustainable energy through vortex-induced vibrations of finite length cylinder," Phys. Fluids **37**(4), 044108 (2025).
[10] H. D. Akaydin, N. G. Elvin, and Y. Andreopoulos, "The performance of a self-excited fluidic energy harvester," Smart Mater. Struct. **21**(2), 025007 (2012).
[11] H. D. Akaydin, N. G. Elvin, and Y. Andreopoulos, "Wake of a cylinder: A paradigm for energy harvesting with piezoelectric materials," Exp. Fluids **49**(2), 291–304 (2010).
[12] U. Javed and A. Abdelkefi, "Characteristics and comparative analysis of piezoelectric-electromagnetic energy harvesters from vortex-induced oscillations," Nonlinear Dyn. **95**, 3309–3333 (2019).
[13] W. Yang, J. Peng, Q. Chen, and S. Zhao, "Advancements and future prospects in ocean wave energy harvesting technology based on micro-energy technology," Micromachines **15**(10), 1199 (2024).
[14] S. Bakhtiar, F. Khan, A. Z. Hajjaj, and H. Fu, "Fluid flow-based vibration energy harvesters: A critical review of state-of-the-art technologies," Appl. Sci. **14**, 11452 (2024).
[15] S. R. Anton and H. A. Sodano, "A review of power harvesting using piezoelectric materials (2003–2006)," Smart Mater. Struct. **16**(3), R1 (2007).
[16] D. Cao, X. Guo, J. Wang, and S. K. Lai, "Recent advancement of flow-induced piezoelectric vibration energy harvesting techniques: Principles, structures, and nonlinear designs," Appl. Math. Mech. **43**, 959–1472 (2022).
[17] P. Han, Q. Huang, G. Pan, D. Qin, W. Wang, R. T. Goncalves, and J. Zhao, "Optimal energy harvesting efficiency from vortex-induced vibration of a circular cylinder," Ocean Eng. **282**, 114869 (2023).
[18] M. Zhang and J. Wang, "Experimental study on piezoelectric energy harvesting from vortex-induced vibrations and wake-induced vibrations," J. Sens. **2016**(1), 2673292.
[19] L. Zhang, A. Abdelkefi, H. Dai, R. Naseer, and L. Wang, "Design and experimental analysis of broadband energy harvesting from vortex-induced vibrations," J. Sound Vib. **408**, 210–219 (2017).
[20] Z. Lai, S. Wang, L. Zhu, G. Zhang, J. Wang, K. Yang, and D. Yurchenko, "A hybrid piezo-dielectric wind energy harvester for high-performance vortex-induced vibration energy harvesting," Mech. Syst. Signal Process. **150**, 107212 (2021).
[21] S. Roundy and P. K. Wright, "A piezoelectric vibration-based generator for wireless electronics," Smart Mater. Struct. **13**(5), 1131–1142 (2004).
[22] H. D. Akaydin, N. Elvin, and Y. Andreopoulos, "Energy harvesting from highly unsteady fluid flows using piezoelectric materials," J. Intell. Mater. Syst. Struct. **21**(13), 1263–1278 (2010).
[23] O. Goushcha, H. D. Akaydin, N. Elvin, and Y. Andreopoulos, "Energy harvesting prospects in turbulent boundary layers," J. Fluids Struct. **54**, 823–847 (2015).
[24] I. Patrick, S. Adhikari, and M. I. Hussein, "Metaharvesting: Emergent energy harvesting by piezoelectric metamaterials," Proc. R. Soc. A **480**, 20240033 (2024).
[25] M. Zhang, C. Zhang, A. Abdelkefi, H. Yu, O. Gaidai, X. Qin, H. Zhu, and J. Wang, "Piezoelectric energy harvesting from vortex-induced vibration of a circular cylinder: Effect of Reynolds number," Ocean Eng. **235**, 109378 (2021).
[26] F. Pan, Z. Xu, P. Pan, and L. Jin, "Piezoelectric energy harvesting from vortex-induced vibration using a modified circular cylinder," in *20th International Conference on Electrical Machines and Systems (ICEMS)* (IEEE, 2017).
[27] M. Verma and A. De, "Dynamics of vortex-induced vibrations of a slit-offset circular cylinder for energy harvesting at low Reynolds number," Phys. Fluids **34**, 083607 (2022).
[28] G. Hu, K. C. S. Kwok, K. T. Tse, and J. Song, "Aerodynamic modification to a circular cylinder to enhance the piezoelectric wind energy harvesting," Appl. Phys. Lett. **109**(19), 193902 (2016).
[29] C. Xia, L. Tang, P. Yin, and K. C. Aw, "Multi-directional and multi-modal vortex-induced vibrations for wind energy harvesting," Appl. Phys. Lett. **125**(20), 203901 (2024).
[30] R. Chatterjee *et al.*, "Energy harvesting from wake-induced vibration of flexible flapper behind a bluff body," Phys. Fluids **36**, 117130 (2024).
[31] R. Chatterjee *et al.*, "Energy harvesting in a flow-induced vibrating flapper with biomimetic gaits," Int. J. Mech. Sci. **272**, 109150 (2024).
[32] I. Borazjani and F. Sotiropoulos, "Vortex-induced vibrations of two cylinders in tandem arrangement in the proximity—Wake interference region," J. Fluid Mech. **621**, 321–364 (2009).
[33] M. M. Zdravkovich and D. L. Pridden, "Interference between two circular cylinders; series of unexpected discontinuities," J. Wind Eng. Ind. Aerodyn. **2**, 255–270 (1977).
[34] J. R. Meneghini, F. Saltara, C. L. R. Siqueira, and J. J. A. Ferrari, "Numerical simulation of flow interference between two circular cylinders in tandem and side-by-side arrangements," J. Fluids Struct. **15**(2), 327 (2001).
[35] J. Mizushima and N. Suehiro, "Instability and transition of flow past two tandem circular cylinders," Phys. Fluids **17**(10), 104107 (2005).
[36] Y. Tasaka, S. Kon, L. Schouveiler, and P. L. Gal, "Hysteretic mode exchange in the wake of two circular cylinders in tandem," Phys. Fluids **18**, 084101 (2006).
[37] P. W. Bearman, "Circular cylinder wakes and vortex-induced vibrations," J. Fluids Struct. **27**, 648–658 (2011).
[38] D. Liu, H. Sun, H. Lin, J. Miao, and H. Liu, "Vortex-induced vibration and energy harvesting in tandem three cylinders with different spacing ratios," Phys. Fluids **37**(1), 017176 (2025).

[39]P. W. Bearman and A. J. Wadcock, "The interaction between a pair of circular cylinders normal to a stream," J. Fluid Mech. **61**, 499–511 (1973).
[40]M. M. Zdravkovich, "Review of interference-induced oscillations in flow past two circular cylinders in various arrangements," J. Wind Eng. Ind. Aerodyn. **28**, 183–199 (1988).
[41]Y. H. Irawan, S. A. Raza, and M.-J. Chern, "Vortex-induced vibration of two circular cylinders in a side-by-side arrangement at moderate Reynolds number: A numerical study," Phys. Fluids **35**(5), 055126 (2023).
[42]S.-X. Guo, M.-T. Song, J.-C. Lei, H.-L. Xu, and C.-C. Chang, "Force element analysis of vortex-induced vibration mechanism of three side-by-side cylinders at low Reynolds number," J. Mar. Sci. Eng. **13**(8), 1446 (2025).
[43]V. Azadeh-Ranjbar, Y. Han, N. Elvin, and Y. Andreopoulos, "Non-linear piezoelectric fluidic energy harvesters: The mutual interaction of two oscillating cylinders," J. Intell. Mater. Syst. Struct. **31**(20), 2378–2389 (2020).
[44]A. Fershalov, N. Elvin, D. Struk, D. M. Romero, P. Orlandini, and Y. Liu, "The effect of endplates on vortex-induced vibration of finite-length cylinders," Phys. Fluids **37**(9), 094139 (2025).
[45]Y. Liao and H. A. Sodano, "Model of a single mode energy harvester and properties for optimal power generation," Smart Mater. Struct. **17**(6), 065026 (2008).
[46]Y. Andreopoulos and A. Honkan, "An experimental study of the dissipative and vortical motion in turbulent boundary layers," J. Fluid Mech. **439**, 131–163 (2001).
[47]C.-K. Choi and D.-K. Kwon, "Wind tunnel blockage effects on aerodynamic behavior of bluff body," Wind Struct. **1**(4), 351–364 (1998).